

¹
² Susceptible host dynamics explain pathogen resilience to
³ perturbations

⁴

⁵ Sang Woo Park, . . . , Bryan T. Grenfell, Sarah Cobey

⁶ Abstract

⁷ A major priority for epidemiological research in the time of anthropogenic change
⁸ is understanding how infectious disease dynamics respond to perturbations. Inter-
⁹ ventions to slow the spread of SARS-CoV-2 significantly disrupted the transmission
¹⁰ of other human pathogens. As interventions lifted, whether and when respiratory
¹¹ pathogens would eventually return to their pre-pandemic dynamics remains to be
¹² answered. Here, we present a framework for estimating pathogen resilience based on
¹³ how fast epidemic patterns return to their pre-pandemic, endemic dynamics and an-
¹⁴ alyze time series data from Hong Kong, Canada, Korea, and the US. By quantifying
¹⁵ the resilience of common respiratory pathogens, we are able to predict when each
¹⁶ pathogen will eventually return to its pre-pandemic, endemic dynamics. Our pre-
¹⁷ dictions closely match the observed deviations (or lack thereof) from its pre-COVID
¹⁸ dynamics. Discrepancies between predicted and observed dynamics indicate the
¹⁹ long-term impact of pandemic perturbations, suggesting that some pathogens may
²⁰ be converging to a different endemic cycle. Finally, we show that the replenishment
²¹ rate of the susceptible pool is a key determinant of pathogen resilience, which in
²² turn determines the sensitivity of a system to stochastic perturbations. Overall, our
²³ analysis highlights the persistent nature of common respiratory pathogens compared
²⁴ to vaccine-preventable infections, such as measles.

25 Non-pharmaceutical interventions to slow the spread of SARS-CoV-2 disrupted
 26 the transmission of other human respiratory pathogens, adding uncertainties to their
 27 future epidemic dynamics and their public health burden [1]. As interventions lifted,
 28 large heterogeneities in outbreak dynamics were observed across different pathogens
 29 in different countries, with some pathogens exhibiting earlier and faster resurgences
 30 than others [2, 3, 4]. Heterogeneities in the overall reduction in transmission and the
 31 timing of re-emergence likely reflect differences in intervention patterns, pathogen
 32 characteristics, immigration/importation from other countries, and pre-pandemic
 33 pathogen dynamics [5]. Therefore, comparing the differential impact of the pan-
 34 *demic* perturbations across pathogens can provide unique opportunities to learn
 35 about underlying pathogen characteristics, such as their transmissibility or duration
 36 of immunity, from heterogeneities in re-emergence patterns [6].

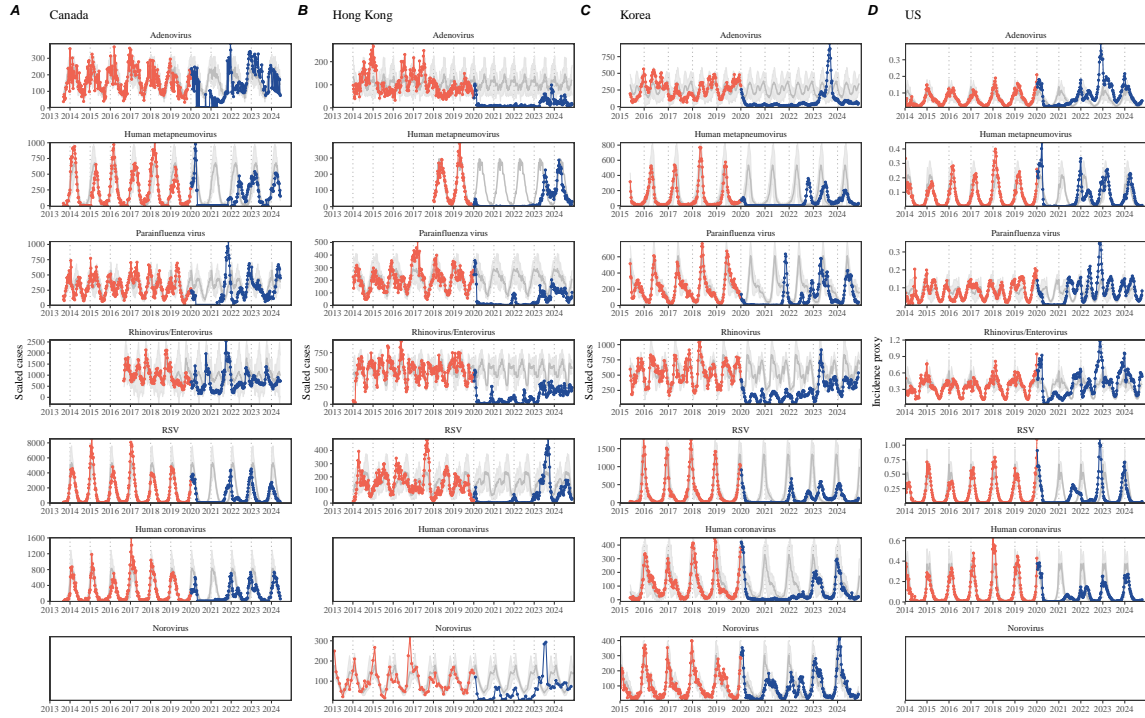


Figure 1: Observed heterogeneity in responses to pandemic perturbations across respiratory pathogens and norovirus in (A) Canada, (B) Hong Kong, (C) Korea, and (D) US. Red points and lines represent data before 2020. Blue points and lines represent data since 2020. Gray lines and shaded regions represent the mean seasonal patterns and corresponding 95% confidence intervals around the mean. Mean seasonal patterns were calculated by aggregating cases before 2020 into 52 weekly bins and taking the average in each week. Cases were scaled to account for changes in testing patterns (Materials and Methods).

37 Even though more than five years have passed since the emergence of SARS-CoV-
 38 2, we still observe persistent changes in pathogen dynamics following the pandemic

39 perturbations. For example, compared to pre-pandemic, seasonal patterns, human
40 metapneumovirus in Korea seem to circulate at lower levels, whereas RSV in Korea
41 seems to exhibit different seasonality (Figure 1). These observations suggest a funda-
42 mental change in pathogen dynamics following the pandemic perturbations, which
43 might be driven by a long-term shift in either human behavior or population-level
44 immunity [7, 8]. For example, the emergence of SARS-CoV-2 could have caused
45 a long-term shift in population-level immunity through its interactions with other
46 pathogens [9], especially with seasonal coronaviruses [7, 10, 11]. The possibility of a
47 long-lasting impact of the pandemic perturbations poses an important question for
48 future infectious disease dynamics: can we predict whether and when other pathogens
49 will eventually return to their pre-pandemic dynamics?

50 So far, most analyses of respiratory pathogens after pandemic perturbations have
51 focused on characterizing the timing of rebound [1, 12, 5]. Instead, we seek to char-
52 acterize how fast (and whether) a pathogen returns to its pre-pandemic dynamics.
53 These two concepts have a subtle but important difference. For example, it took
54 more than 3 years for human metapneumovirus to rebound in Hong Kong, but the
55 observed epidemic patterns in 2024 are similar to pre-pandemic seasonal means, sug-
56 gesting a rapid return to pre-pandemic dynamics (Figure 1). Measuring this rate of
57 return is useful because it allows us to quantify the ecological resilience of a host-
58 pathogen system, which can inform responses to future interventions [13, 14, 15, 16].

59 In this study, we lay out theoretical and statistical approaches to characterizing
60 the resilience of a host-pathogen system based on how fast the system recovers from
61 perturbation. We begin by laying out a few representative scenarios that capture the
62 potential impact of pandemic perturbations on endemic pathogen dynamics and illus-
63 trate how resilience can be measured by comparing the pre- and post-pandemic dy-
64 namics of susceptible and infected hosts. In practice, information on susceptible hosts
65 is often unavailable, making this theoretical approach infeasible. Instead, we utilize a
66 mathematical technique to reconstruct empirical attractors from the data [17], which
67 allows us to measure the rate at which the host-pathogen system approaches this em-
68 pirical attractor after a perturbation; this rate corresponds to the resilience of the
69 host-pathogen system. We use this method to analyze pathogen surveillance data for
70 respiratory and non-respiratory pathogens from Canada, Hong Kong, Korea, and the
71 US. Finally, we show that susceptible host dynamics explain variation in pathogen
72 resilience and further demonstrate that more resilient pathogens will be less sensitive
73 to perturbations caused by demographic stochasticity, thereby providing a direct link
74 between pathogen resilience and persistence.

75 **Conceptual introduction to pathogen resilience**

76 In classical ecological literature, the resilience of an ecological system is measured by
77 the rate at which the system returns to its reference state following a perturbation
78 [13, 14, 15, 16]. This rate corresponds to the largest real part of the eigenvalues of

79 the linearized system near equilibrium—here, we refer to this value as the *intrinsic*
80 resilience of the system, which represents the expected rate of return from perturbed
81 states. In practice, we rarely know the true model describing population-level dy-
82 namics of common respiratory pathogens, limiting our ability to infer the intrinsic
83 resilience of a system. Instead, we can still measure the *empirical* resilience of a
84 host-pathogen system by looking at how fast the system returns to the pre-pandemic,
85 endemic dynamics after pandemic perturbations are lifted.

86 As an example, we begin with a simple Susceptible-Infected-Recovered-Susceptible
87 (SIRS) model with seasonally forced transmission and demography (i.e., birth and
88 death). The SIRS model is the simplest model that allows for the waning of im-
89 munity and is commonly used for modeling the dynamics of respiratory pathogens
90 [18]. First, consider a pandemic perturbation that reduces transmission by 50% for 6
91 months starting in 2020, which causes epidemic patterns to deviate from their origi-
92 nal stable annual cycle for a short period of time and eventually come back (Figure
93 2A). To measure the resilience of this system empirically, we first need to be able to
94 measure the distance from its pre-pandemic attractor. There are many ways we can
95 measure the distance from the attractor, but for illustrative purposes, we choose one
96 of the most parsimonious approaches: that is, we look at how the susceptible (S) and
97 infected (I) populations change over time and measure the distance on the SI phase
98 plane (Figure 2B). In this simple case, the locally estimated scatterplot smoothing
99 (LOESS) fit indicates that the distance from the attractor decreases exponentially
100 (linearly on a log scale) on average (Figure 2C). Furthermore, the overall rate of re-
101 turn approximates the intrinsic resilience of the seasonally unforced system (Figure
102 2C).

103 Alternatively, pandemic perturbations can have a lasting impact on the pathogen
104 dynamics; as an example, we consider a scenario in which a 10% reduction in trans-
105 mission persists even after the major pandemic perturbations are lifted (Figure 2D–
106 F). In such cases, we cannot know whether the pathogen will return to its original
107 cycle or a different cycle until many years have passed, and we cannot measure the
108 distance to the new unknown attractor that the system might eventually approach.
109 Nonetheless, we can still measure the distance from the pre-pandemic attractor and
110 ask how the distance changes over time (Figure 2E). The LOESS fit suggests that the
111 distance from the pre-pandemic attractor will initially decrease exponentially on av-
112 erage (equivalently, linearly on a log scale) and eventually plateau (Figure 2F). Here,
113 a permanent 10% reduction in transmission rate slows the system, which causes the
114 distance from the pre-pandemic attractor initially to decrease at a slower rate (Figure
115 2F) than it would have otherwise (Figure 2C) before plateauing at a fixed distance
116 between the two attractors. This example shows that resilience is not necessarily an
117 intrinsic property of a specific pathogen. Instead, pathogen resilience is a property
118 of a specific attractor that a host-pathogen system approaches, which depends on
119 both pathogen and host characteristics.

120 Finally, transient phenomena can further complicate the picture (Figure 2G–I).
121 For example, a stage-structured model initially exhibits a stable annual cycle, but

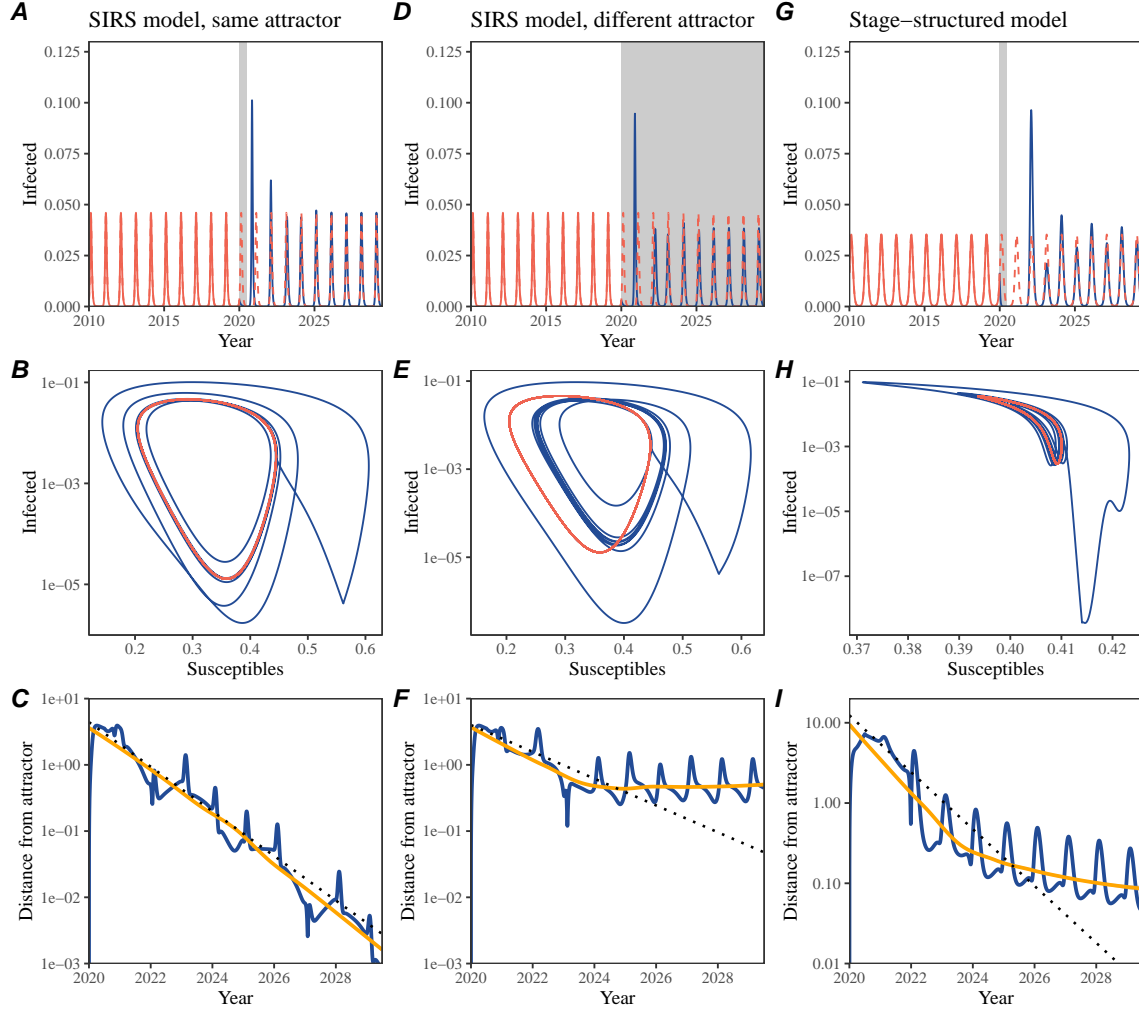


Figure 2: A simple method to measure pathogen resilience following pandemic perturbations across different scenarios. (A, D, G) Simulated epidemic trajectories across various models. Red and blue solid lines represent epidemic dynamics before and after pandemic perturbations are introduced, respectively. Red dashed lines represent counterfactual epidemic dynamics in the absence of perturbations. Gray regions indicate the duration of perturbations. (B, E, H) Phase plane representation of the time series in panels A, D, and G alongside the corresponding susceptible host dynamics. Red and blue solid lines represent epidemic trajectories on an SI phase plane before and after perturbations are introduced, respectively. (C, F, I) Changes in logged distance from the attractor over time. Blue lines represent the logged distance from the attractor. Orange lines represent the locally estimated scatterplot smoothing (LOESS) fits to the logged distance from the attractor. Dotted lines show the intrinsic resilience of the seasonally unforced system.

122 perturbations from a 10% reduction in transmission for 6 months cause the epidemic

123 to shift to biennial cycles (Figure 2G). The system eventually approaches the original
124 pre-pandemic attractor (Figure 2H), suggesting that this biennial cycle is a transient
125 phenomenon. The LOESS fit indicates that the distance from the attractor initially
126 decreases exponentially at a rate that is consistent with the intrinsic resilience of
127 the seasonally unforced stage-structured system, but the rate of decrease decelerates
128 with the damped oscillations (Figure 2I). This behavior is also referred to as a ghost
129 attractor, which causes long transient dynamics and slow transitions [19]. Strong
130 seasonal forcing in transmission can also lead to transient phenomena for a simple
131 SIRS model, causing a slow return to pre-perturbation dynamics (Supplementary
132 Figure S1).

133 This empirical approach allows us to measure the resilience of a two-strain host-
134 pathogen system even when we have incomplete observation of the infection dynam-
135 ics. Simulations from a simple two-strain competition system illustrate that separate
136 analyses of individual strain dynamics (e.g., RSV A vs B) and a joint analysis of total
137 infections (e.g., total RSV infections) yield identical resilience estimates (Supplemen-
138 tary Figure S2, 3). This is expected because the dynamics of two strains (or two
139 pathogens) around the attractor in a coupled system are described by the same set
140 of eigenvalues and eigenvectors, meaning that both strains should exhibit identical
141 rates of returns following a perturbation. Analogous to a single system, strong sea-
142 sonal forcing in transmission can cause the system to slow down through transient
143 phenomena (Supplementary Figure S4).

144 These observations yield three insights. First, we can directly estimate the empirical
145 resilience of a host-pathogen system by measuring the rate at which the system
146 approaches an attractor, provided that we have a way to quantify the distance from
147 the attractor. The empirical approach to estimating pathogen resilience is particu-
148 larly convenient because it does not require us to know the true underlying model;
149 estimating the intrinsic resilience from fitting misspecified models can lead to biased
150 estimates (Supplementary Figure S5). Second, resilience estimates allow us to make
151 phenomenological predictions about the dynamics of a host-pathogen system follow-
152 ing a perturbation. Assuming that an attractor has not changed and the distance
153 from the attractor will decrease exponentially over time, we can obtain a ballpark
154 estimate for when the system should reach an attractor. Finally, a change in the rate
155 of an exponential decrease in the distance from the attractor can provide information
156 about whether the system has reached an alternative attractor, or a ghost attractor,
157 that is different from the original, pre-pandemic attractor. These alternative attrac-
158 tors may reflect continued perturbations from permanent changes in transmission
159 patterns as well as changes in immune landscapes. There will be periods of time
160 when it is difficult to tell whether pathogen dynamics are still diverging from the
161 original attractor or have begun to converge to a new attractor; now that several
162 years have passed since interventions have been lifted, we expect many respiratory
163 pathogens to have had sufficient time to begin returning to their post-intervention
164 attractors. With recent data, we can start to evaluate whether we see early signs of
165 convergence to the former attractor or a new one.

166 **Inferring pathogen resilience from real data**

167 Based on these observations, we now lay out our approach to estimating pathogen
168 resilience from real data (Figure 3). We first tested this approach against simulations
169 and applied it to real data. Specifically, we analyzed case time series of respiratory
170 pathogens from four countries: Canada, Hong Kong, Korea, and the US.

171 So far, we have focused on simple examples that assume a constant transmission
172 reduction during the pandemic. However, in practice, the impact of pandemic per-
173 turbations on pathogen transmission was likely more complex (Figure 3A), reflecting
174 introduction and relaxation of various intervention strategies. In some cases, strong
175 perturbations likely caused local fadeouts, requiring immigration from another loca-
176 tion for epidemic rebound. Such complexities could lead to longer delays between
177 the introduction of pandemic perturbations and pathogen rebound as well as tempo-
178 ral variation in outbreak sizes (Figure 3B): in this example, continued transmission
179 reduction from interventions limits the size of the first outbreak in 2021 following
180 the rebound, allowing for a larger outbreak in 2022 when interventions are further
181 relaxed.

182 Previously, we relied on the dynamics of susceptible and infected hosts to com-
183 pute the distance from the attractor (Figure 2), but information on susceptible hosts
184 is rarely available in practice. In addition, uncertainties in case counts due to ob-
185 servation error, strain evolution, and multiannual cycles in the observed epidemic
186 dynamics (e.g., adenovirus circulation patterns in Hong Kong and Korea) add chal-
187 lenges to defining pre-pandemic attractors, which limits our ability to measure the
188 distance from the attractor. To address these challenges, we can reconstruct an em-
189 pirical attractor by utilizing Takens' theorem [17], which states that an attractor of a
190 nonlinear multidimensional system can be mapped onto a delayed embedding (Mate-
191 rials and Methods). For example, we can use delayed logged values of pre-pandemic
192 cases $C(t)$ (Figure 3C) to reconstruct the attractor:

$$\langle \log(C(t) + 1), \log(C(t - \tau) + 1), \dots, \log(C(t - (M - 1)\tau) + 1) \rangle, \quad (1)$$

193 where the delay τ and embedding dimension M are determined based on autocor-
194 relations and false nearest neighbors, respectively [20, 21]. We can then apply the
195 same delay and embedding dimensions to the entire time series to determine the po-
196 sition in multi-dimensional state space (Figure 3D), which allows us to measure the
197 nearest neighbor distance between the current state of the system and the empirical
198 pre-pandemic attractor (Figure 3E). In theory, we can now quantify how fast this
199 distance decreases by fitting a linear regression on a log scale, where the slope of
200 the linear regression empirically measures pathogen resilience. However, resulting
201 estimates of pathogen resilience can be sensitive to choices about embedding delays
202 and dimensions. For example, using longer delays and higher dimensions tends to
203 smooth out temporal variations in the distance from the attractor (Supplementary
204 Figure S6).

205 Complex changes in the distance from the attractor suggest that estimating

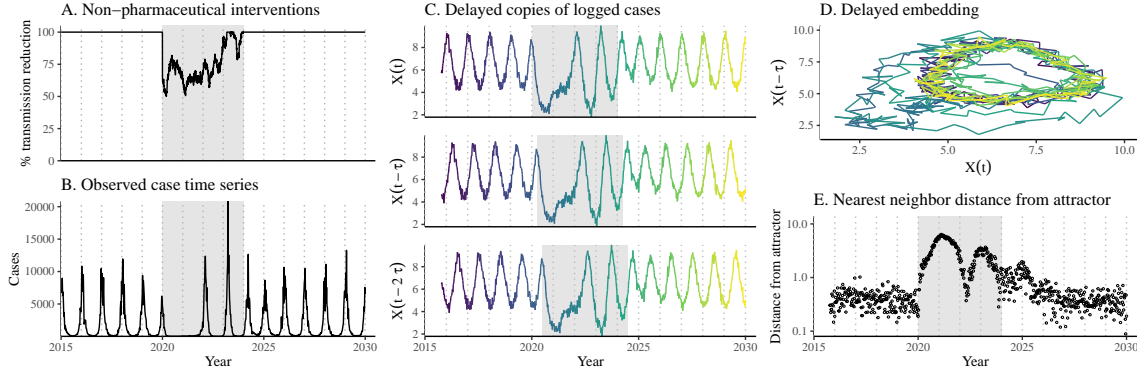


Figure 3: **A schematic diagram explaining the inference of pathogen resilience from synthetic data.** (A) A realistic example of simulated pandemic perturbations, represented by a relative reduction in transmission. (B) The impact of the synthetic pandemic perturbation on epidemic dynamics simulated using a SIRS model with demographic stochasticity. (C) Generating delayed copies of the logged time series allows us to obtain an embedding. (D) Two dimensional representation of an embedding. (E) Delayed embedding allows us to calculate the nearest neighbor distance from the empirical attractor, which is determined based on the pre-pandemic time series. This distance time series can be used to infer pathogen resilience after choosing an appropriate window for linear regression.

206 pathogen resilience from linear regression will be particularly sensitive to our choice
 207 of fitting windows for the regression (Figure 3E). Therefore, before we tried estimat-
 208 ing resilience from real data, we explored an automated window selection criterion
 209 for linear regression and tested it against randomized, stochastic simulations across
 210 a range of realistic pandemic perturbation shapes. In doing so, we also explored
 211 optimal choices for embedding dimensions and evaluated our choices of fitting win-
 212 dow parameters and embedding dimensions by quantifying correlation coefficients
 213 between the estimated resilience and the intrinsic resilience of a seasonally unforced
 214 system (Materials and Methods). Overall, we found large variation in estimation
 215 performances with correlation coefficient ranging from 0.21 to 0.61 (Supplementary
 216 Figure S7). In almost all cases, the automated window selection approach outper-
 217 formed a naive approach that uses the time series, starting from the peak distance
 218 (Supplementary Figure S7).

219 Based on the best performing window selection criteria and embedding dimen-
 220 sion, we applied this approach to pathogen surveillance data presented in Figure
 221 1 (Materials and Methods). For each time series, we applied Takens' theorem in-
 222 dependently to reconstruct the empirical attractor and obtained the corresponding
 223 time series of distances from attractors (Supplementary Figure S8). Then, we used
 224 the automated window selection criterion to fit a linear regression and estimated the
 225 empirical resilience for each pathogen in each country (Supplementary Figure S8);
 226 the window selection criterion gave poor regression window for three cases (norovirus

227 in Hong Kong and Korea and rhinovirus/enterovirus in the US), leading to unrealistically low resilience estimates, and so we used ad-hoc regression windows instead
228 (Supplementary Figure S9; Materials and Methods).

230 For all pathogens we considered, resilience estimates fell between 0.4/year and
231 1.8/year (Figure 4A). We estimated the mean resilience of common respiratory
232 pathogens to be 0.99/year (95% CI: 0.81/year–1.18/year). For reference, this is
233 \approx 7.5 times higher than the intrinsic resilience of pre-vaccination measles in England
234 and Wales (\approx 0.13/year). Finally, resilience estimates for norovirus were comparable
235 to those of common respiratory pathogens: 1.44/year (95%CI: 1.01/year–1.87/year)
236 for Hong Kong and 1.07/year (95%CI: 0.86/year–1.29/year) for Korea. Based on
237 a simple ANOVA test, we did not find significant differences in resilience estimates
238 across countries ($p = 0.25$) or pathogens ($p = 0.67$).

239 Using resilience estimates, we predicted when each pathogen would hypothetically
240 return to their pre-pandemic dynamics, assuming no long-term change in the attractor.
241 Specifically, we extended our linear regression fits to distance-from-attractor
242 time series and ask when the predicted regression line will cross a threshold value;
243 since we relied on nearest neighbor distances, pre-pandemic distances are always
244 greater than zero (Figure 3E), meaning that we can use the mean of pre-pandemic
245 distances as our threshold.

246 We predicted that a return to pre-pandemic cycles has occurred would be im-
247 minent for most pathogens (Figure 4B). In particular, we predicted that 12 out of
248 23 pathogen-country pairs should have already returned before the end of 2024. For
249 almost all pathogens that were predicted to have returned already, the observed
250 epidemic dynamics showed clear convergence towards their pre-pandemic seasonal
251 averages, confirming our predictions (Figure 4C). However, there were a few ex-
252 ceptions, including norovirus in Hong Kong and rhinovirus/enterovirus in the US,
253 where the observed epidemic dynamics in 2024 exhibit clear deviation from their pre-
254 pandemic seasonal averages (Figure 4C; Figure S9). These observations suggest a
255 possibility that some common respiratory pathogens may have converged to different
256 attractors or are still exhibiting non-equilibrium dynamics. In contrast, pathogens
257 that were predicted to have not returned yet also showed clear differences from their
258 pre-pandemic seasonal averages; as many of these pathogens are predicted to return
259 in 2025–2026, we may be able to test these predictions in near future (Supplementary
260 Figure S10). Our reconstructions of distance time series and estimates of pathogen
261 resilience and expected return time were generally robust to choices of embedding
262 dimensions (Supplementary Figure S11–12).

263 **Susceptible host dynamics explain variation in pathogen 264 resilience**

265 So far, we have focused on quantifying pathogen resilience from the observed pat-
266 terns of pathogen re-emergence following pandemic perturbations. But what factors

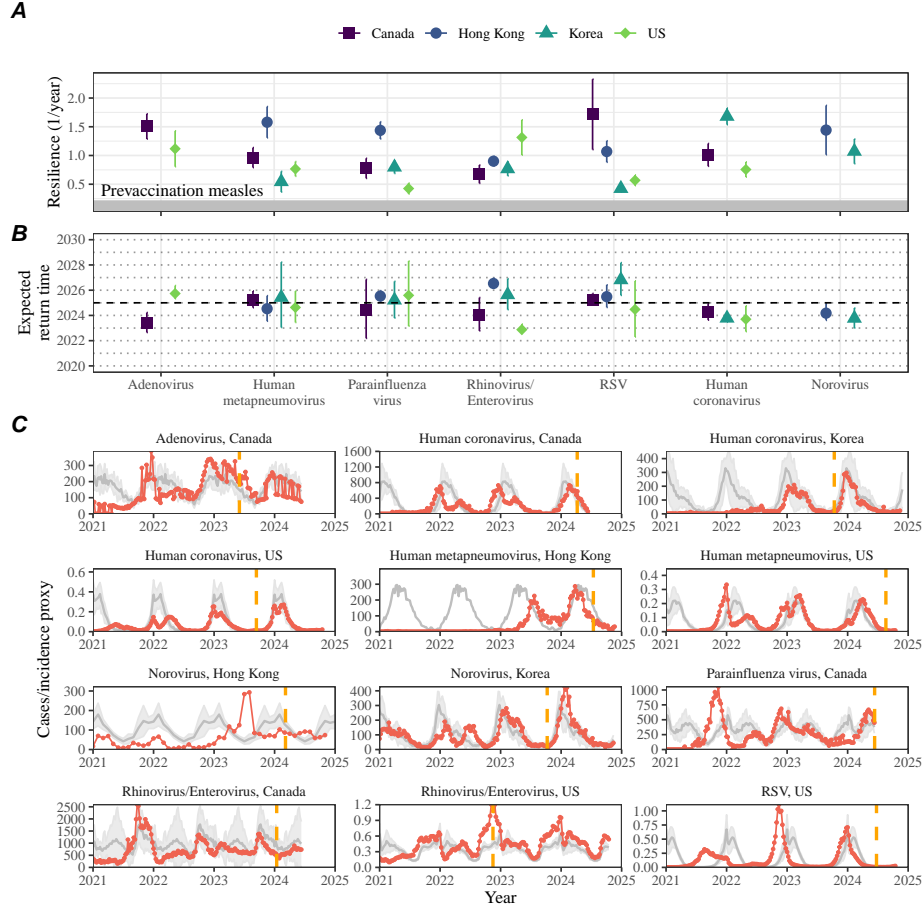


Figure 4: **Summary of resilience estimates and predictions for return time.** (A) Estimated pathogen resilience. The gray horizontal line represents the intrinsic resilience of pre-vaccination measles dynamics. (B) Predicted timing of when each pathogen will return to their pre-pandemic cycles. The dashed line in panel B indicates the end of 2024. Error bars represent 95% confidence intervals. (C) Observed dynamics for pathogen that are predicted to have returned before the end of 2024. Red points and lines represent data before 2020. Gray lines and shaded regions represent the mean seasonal patterns and corresponding 95% confidence intervals around the mean, previously shown in Figure 1. Orange vertical lines represent the predicted timing of return.

determine how resilient a host-pathogen system is? To address this question, we used the SIRS model to explore how changes in susceptible host dynamics affect pathogen resilience. To do so, we varied the basic reproduction number \mathcal{R}_0 , which represents the average number of secondary infections caused by a newly infected individual in a fully susceptible population, and the duration of immunity and computed intrinsic resilience for each parameter.

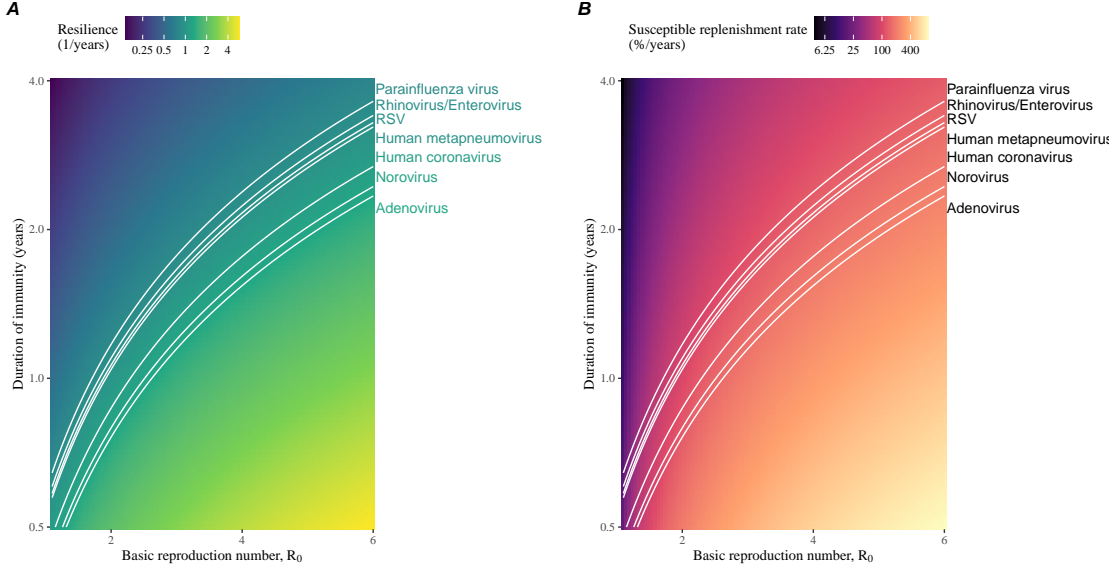


Figure 5: Linking pathogen resilience to epidemiological parameters and susceptible host dynamics. (A) Intrinsic resilience as a function of the basic reproduction number \mathcal{R}_0 and the duration of immunity. (B) Per-capita susceptible replenishment rate as a function of the basic reproduction number \mathcal{R}_0 and the duration of immunity. The standard SIRS model without seasonal forcing is used to compute intrinsic resilience and the per-capita susceptible replenishment rate. Lines correspond to a set of parameters that are consistent with mean resilience estimates for each pathogen, averaged across different countries.

We found that an increase in \mathcal{R}_0 and a decrease in the duration of immunity correspond to an increase in pathogen resilience (Figure 5A). Similarly, an increase in \mathcal{R}_0 and a decrease in the duration of immunity corresponds to a faster per-capita rate of susceptible replenishment, which is defined as the ratio between absolute rate at which new susceptibles enter the population and the equilibrium number of susceptible individuals in the population, S^* (Figure 5B). We note that a higher \mathcal{R}_0 drives a faster per-capita susceptible replenishment rate by decreasing the susceptible proportion at equilibrium, S^* . For a simple SIR model that assumes a life-long immunity, we can show analytically that pathogen resilience is proportional to the per-capita rate of susceptible replenishment (Materials and Methods). Overall, these observations suggest that a faster per-capita susceptible replenishment rate causes the system to be more resilient.

By taking the average values of empirical resilience values for each pathogen, we were able to map each pathogen onto a set of parameters of the SIRS model that are consistent with corresponding resilience estimates (Figure 5A). Across all pathogens we considered, we estimated that the average duration of immunity is likely to be short (< 4 years) across a plausible range of \mathcal{R}_0 (< 6). We were also able to obtain

²⁹⁰ a plausible range of susceptible replenishment rates for each pathogen (Figure 5B),
²⁹¹ but there was a large uncertainty in the estimates for susceptible replenishment rates
²⁹² due to a lack of one-to-one correspondence between susceptible replenishment rates
²⁹³ and pathogen resilience.

²⁹⁴ **Pathogen resilience determines sensitivity to stochastic perturbations**

²⁹⁵ Beyond the pandemic perturbations, we hypothesized host-pathogen systems to experience continued perturbations of varying degrees from changes in epidemiological conditions, such as human behavior, climate, and viral evolution. These perturbations can also arise from demographic stochasticity, which is inherent to any ecological systems. Here, we used a seasonally unforced SIRS model with birth/death to explore how resilience of a host-pathogen system determines the sensitivity to perturbations caused by demographic stochasticity (Materials and Methods).

³⁰³ We found that resilience of a host-pathogen system determines the amount of deviation from the deterministic trajectory caused by demographic stochasticity, with less resilient systems experiencing larger deviations (Figure 6). Notably, less resilience systems also exhibited slower epidemic cycles (Figure 6A–C). The periodicity of this epidemic cycle matched those predicted by the intrinsic periodicity of the system (Supplementary Figure S13) where the intrinsic resilience of the system is inversely proportional to its intrinsic periodicity (Supplementary Figure S14).

³¹⁰ These conclusions were robust for the seasonally forced SIRS model (Supplementary Figure S15).

³¹² **Discussion**

³¹³ COVID-19 pandemic interventions caused major disruptions to circulation patterns of both respiratory and non-respiratory pathogens, adding challenges to predicting their future dynamics [1, 2, 3, 4]. However, these perturbations offer large-scale natural experiments for understanding how different pathogens respond to perturbations. In this study, we showed that pathogen re-emergence patterns following pandemic perturbations can be characterized through the lens of ecological resilience. We showed that variation in pathogen resilience can be explained by the differences in susceptible host dynamics, where faster replenishment of the susceptible pool corresponds to a more resilient host-pathogen system. Finally, we showed that pathogen resilience also determines the sensitivity to stochastic perturbations.

³²³ We analyzed case time series of common respiratory infections and norovirus infections from Canada, Hong Kong, Korea, and the US to estimate their resilience. Overall, we estimated the resilience of these pathogens to range from 0.4/year to 1.8/year, which is 3–14 times more resilient than prevaccination measles. These

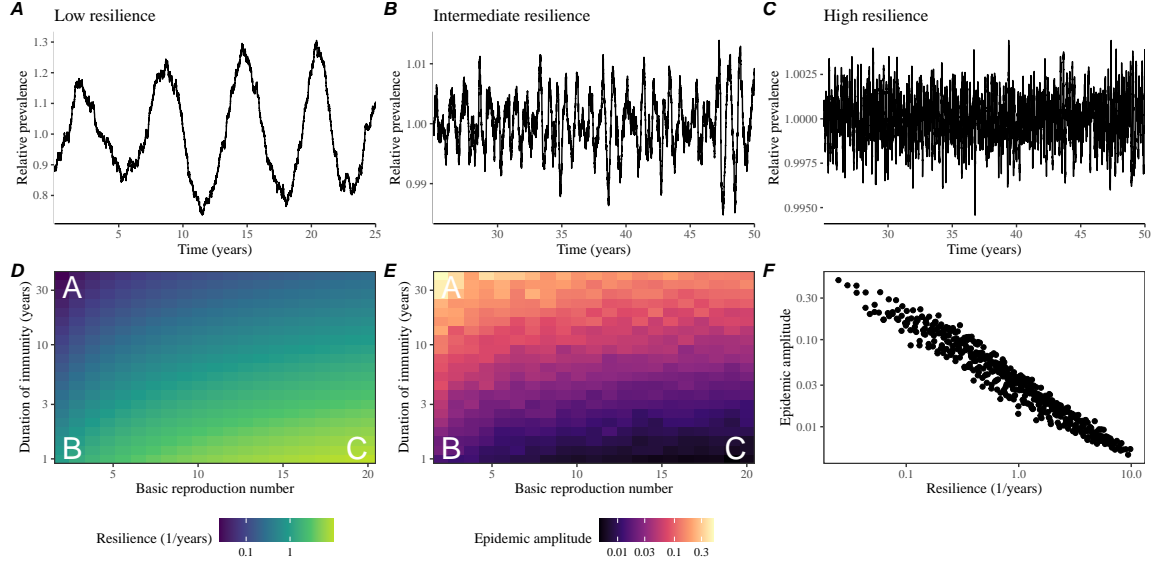


Figure 6: Linking resilience of a host-pathogen system to its sensitivity to stochastic perturbations. (A–C) Epidemic trajectories of a stochastic SIRS model across three different resilience values: low, intermediate, and high. The relative prevalence was calculated by dividing infection prevalence by its mean value. (D) The heat map represents the intrinsic resilience of a system as a function of the basic reproduction number \mathcal{R}_0 and the duration of immunity. (E) The heat map represents the epidemic amplitude as a function of the basic reproduction number \mathcal{R}_0 and the duration of immunity. The epidemic amplitude corresponds to $(\max I - \min I)/(2\bar{I})$, where \bar{I} represents the mean prevalence. (F) The relationship between pathogen resilience and epidemic amplitude.

resilience estimates indicate that common respiratory pathogens and norovirus likely exhibit faster susceptible replenishment and are therefore more persistent, indicating potential challenges in controlling these pathogens.

Based on our resilience estimates, we made phenomenological predictions about when each pathogen will return to their endemic cycles. For the most part, we accurately predicted which pathogens should have already returned before the end of 2024. However, there were few exceptions (i.e., norovirus in Hong Kong and rhinovirus/enterovirus in the US), suggesting a possibility that these may have converged to different endemic cycles compared to their pre-pandemic epidemic patterns. These changes may reflect changes in surveillance or actual shift in the dynamics, caused by permanent changes in behavior or population-level immunity. While it may seem unlikely that permanent changes in behavior would only affect a few pathogens and not others, we cannot rule out this possibility given heterogeneity in the age of infection across different respiratory pathogens [22, 23]. Differences in the mode of transmission between respiratory vs gastrointestinal pathogens may also contribute

342 to the differences in responses to pandemic perturbations. However, it is unclear
343 why norovirus dynamics in Korea seemed to have returned, whereas those in Hong
344 Kong have not.

345 For almost half of the pathogens we considered, we predicted that their return
346 to original epidemic patterns is imminent. We will need a few more years of data
347 to test whether these pathogens will eventually return to their original dynamics
348 or eventually converge to a different attractor. Overall, these observations echo
349 earlier studies that highlighted the long-lasting impact of pandemic perturbations
350 [8, 24, 25, 4].

351 We showed that susceptible host dynamics shape pathogen resilience, where faster
352 replenishment of the susceptible population causes the pathogen to be more resilient.
353 For simplicity, we focus on waning immunity and birth as the main drivers of the
354 susceptible host dynamics but other mechanisms can also contribute to the replen-
355 ishment of the susceptible population. In particular, pathogen evolution, especially
356 the emergence of antigenically novel strains, can cause effective waning of immunity
357 in the population; therefore, we hypothesize that faster rates of antigenic evolution
358 can also cause a pathogen to be more resilient. Future studies should explore the
359 relationship between the rate of evolution and resilience for antigenically evolving
360 pathogens.

361 Quantifying pathogen resilience also offers novel approaches to validating population-
362 level epidemiological models. So far, most of model validation in infectious disease
363 ecology is based on the ability of a model to reproduce the observed epidemic dy-
364 namics and to predict future dynamics [26, 27, 28, 29, 30]. However, many models
365 can perform similarly under these criteria. For example, two major RSV models
366 have been proposed to explain biennial epidemic patterns: (1) a stage- and age-
367 structured model that allows disease severity to vary with number of past infections
368 and age of infection [28] and (2) a pathogen-interaction model that accounts for cross
369 immunity between RSV and human metapneumovirus [27]. Since both models can
370 accurately reproduce the observed epidemic patterns, standard criteria for model
371 validation do not allow us to distinguish between these two models from population-
372 level data alone. Instead, it would be possible to measure the empirical resilience of
373 each model by simulating various perturbations and compare them to estimates of
374 empirical resilience from data, using pandemic perturbations as an opportunity.

375 There are several limitations to our work. First, we did not extensively explore
376 other approaches to reconstructing the attractor. Recent studies showed that more
377 sophisticated approaches, such as using non-uniform embedding, can provide more
378 robust reconstruction for noisy data [21]. In the context of causal inference, choices
379 about embedding can have major impact on the resulting inference [31]. Our re-
380 silience estimates are likely overly confident given a lack of uncertainties in attractor
381 reconstruction as well as the simplicity of our statistical framework. Nonetheless,
382 as illustrated in our sensitivity analyses, inferences about pathogen resilience in our
383 SIRS model appear to be robust to decisions about embedding lags and dimensions—
384 this is because tracking the rate at which the system approaches the attractor is

likely a much simpler problem than making inferences about causal directionality. Short pre-pandemic time series also limit our ability to accurately reconstruct the attractor and contribute to the crudeness of our resilience estimates; although this is less likely a problem for respiratory pathogens that are strongly annual, our attractor reconstruction may be inaccurate for those exhibiting multi-annual cycles, such as adenovirus in Hong Kong and Korea. Uncertainties in pathogen dynamics due to changes in testing patterns further contribute to the curdeness of our resilience estimates. Despite these limitations, our qualitative prediction that common respiratory pathogens are more resilient than prevaccination measles is also likely to be robust, given how rapid many respiratory pathogens returned to their original cycles following pandemic perturbations.

Predicting the impact of anthropogenic changes on infectious disease dynamics is a fundamental aim of infectious disease research in a rapidly changing world. Our study illustrates that how a host-pathogen system responds to both small and large perturbations is largely predictable through the lens of ecological resilience. In particular, quantifying the resilience of a host-pathogen system offers a unique insight into questions about endemic pathogens' responses to pandemic perturbations, including whether some pathogens will exhibit long-lasting impact from the pandemic perturbation or not. More broadly, a detailed understanding of the determinants of pathogen resilience can provide deeper understanding of pathogen persistence.

Materials and Methods

Data

We gathered time series on respiratory infections from Canada, Hong Kong, Korea, and United States (US). As a reference, we also included time series data on norovirus infections for available countries. In contrast to respiratory pathogens, we expect gastrointestinal viruses, such as norovirus, to be differently affected by pandemic perturbations.

Weekly time series of respiratory infection cases in Canada comes from a publicly available website by the Respiratory Virus Detection Surveillance System, which collect data from select laboratories across Canada [32]. Weekly time series of respiratory infection cases in Hong Kong comes from a publicly available website by the Centre for Health Protection, Department of Health [33, 34]. Weekly time series of acute respiratory infection cases in Korea comes from a publicly available website by the Korea Disease Control and Prevention Agency [35]. Finally, weekly time series of respiratory infection cases in the US were obtained from the National Respiratory and Enteric Virus Surveillance System. Time series on number of tests were also available in Canada, Hong Kong, and the US, but not in Korea. [SWP: Not sure how to cite NREVSS data because we got it by emailing them...]

423 **Data processing**

424 For all time series, we rounded every year to 52 weeks by taking the average number
425 of cases and tests between the 52nd and 53rd week. We also rescale all time series to
426 account for changes in testing patterns, which are then used for the actual analysis.

427 For Canada, an increase in testing was observed from 2013 to 2024 (Supplemental
428 Figure S15). To account for this increase, we calculated a 2 year moving average
429 for the number of tests for each pathogen, which we used as a proxy for testing effort.
430 Then, we divided the smoothed testing patterns by the smoothed value at the final
431 week such that the testing effort has a maximum of 1. We then divided weekly cases
432 by the testing effort to obtain a scaled case time series. A similar approach was used
433 earlier for an analysis of RSV time series in the US to account for changes in testing
434 patterns [28].

435 For Hong Kong, we also applied the same scaling procedure to the time series
436 as we did for Canada. In this case, we only adjusted for testing efforts up to the
437 end of 2019 because there was a major reduction in testing for common respiratory
438 pathogens since 2020 (Supplementary Figure S16).

439 For Korea, while we did not have information on testing, the reported number
440 of respiratory infections consistently increased from 2013 to the end of 2019, which
441 we interpreted as changes in testing patterns (Supplementary Figure S17). Since
442 we did not have testing numbers, we used the weekly sum of all acute respiratory
443 viral infection cases as a proxy for testing, which were further smoothed with moving
444 averaged and scaled to have a maximum of 1. For Korea, we also only adjusted for
445 testing efforts up to the end of 2019.

446 In the US, there has been a large increase in testing against some respiratory
447 pathogens, especially RSV, which could not be corrected for through simple scaling
448 (Supplementary Figure S18). Instead, we derived an incidence proxy by multiplying
449 the test positivity with influenza-like illness positivity, which was taken from
450 <https://gis.cdc.gov/grasp/fluvview/fluportaldashboard.html>. This method
451 of estimating an incidence proxy has been recently applied in the analysis of seasonal
452 coronaviruses [7] and *Mycoplasma pneumoniae* infections [4]. Detailed assumptions
453 and justifications are provided in [36].

454 **Data summary**

455 To make qualitative comparisons between pre- and post-perturbation dynamics of
456 respiratory pathogen circulation patterns, we calculate the mean seasonal patterns
457 using time series of either rescaled cases or incidence proxy estimates before 2020. We
458 do so by taking the mean value in each week across all years before 2020. Confidence
459 intervals around the means are calculated using a simple t test.

460 **Estimating pathogen resilience**

461 In order to measure pathogen resilience from surveillance data, we first reconstructed
 462 the empirical pre-pandemic attractor of the system using Takens' embedding theorem
 463 [17]. Specifically, for a given pathogen, we took the pre-pandemic (before 2020)
 464 case time series $C(t)$ and reconstruct the attractor using delayed embedding with a
 465 uniform delay of τ and dimension M :

$$X_{\tau,m}(t) = \langle \log(C(t) + 1), \log(C(t - \tau) + 1), \dots, \log(C(t - (M-1)\tau) + 1) \rangle. \quad (2)$$

466 Here, the delay τ was determined by calculating the autocorrelation of the logged
 467 pre-pandemic time series and asking when the autocorrelation crosses 0 for the first
 468 time [21]; a typical delay for an annual outbreak is around 13 weeks.

469 Then, for a given delay τ , we determined the embedding dimension M using the
 470 false nearest neighbors approach [20, 21]. To do so, we started with an embedding
 471 dimension e and construct a set of points $A_{\tau,e} = \{X_{\tau,e}(t) | t < 2020\}$. Then, for
 472 each point $X_{\tau,e}(t)$, we determined the nearest neighbor from the set $A_{\tau,e}$, which we
 473 denote $X_{\tau,e}(t_{nn})$ for $t \neq t_{nn}$. Then, if the distance between these two points on $e+1$
 474 dimension, $D_{\tau,e+1}(t) = \|X_{\tau,e+1}(t_{nn}) - X_{\tau,e+1}(t)\|_2$, is larger than their distance on
 475 e dimension, $D_{\tau,e}(t) = \|X_{\tau,e}(t_{nn}) - X_{\tau,e}(t)\|_2$, these two points are deemed to be
 476 false nearest neighbors; specifically, we used a threshold R for the ratio between
 477 two distances $D_{\tau,e+1}(t)/D_{\tau,e}(t)$ to determine false nearest neighbors. For the main
 478 analysis, we used $R = 10$, which was chosen from a sensitivity analysis against
 479 simulated data (Supplementary Text). Once we determined the embedding lag τ
 480 and dimension M , we apply the embedding to the entire time series and calculate
 481 the nearest neighbor distance against the attractor $A_{\tau,M}$ to obtain a time series of
 482 distance from the attractor $D_{\tau,M}(t)$.

483 From a time series of distances from the attractor, we estimated pathogen re-
 484 silience by fitting a linear regression to an appropriate window. To automatically se-
 485 lect the fitting window, we began by smoothing the distance time series using locally
 486 estimated scatterplot smoothing (LOESS) to obtain $\hat{D}_{\tau,M}(t)$, where the smoothing
 487 is performed on a log scale and exponentiated afterwards. Then, we determined
 488 threshold values (T_{start} and T_{end}) for the smoothed distances and choose the fitting
 489 window based on when $\hat{D}_{\tau,M}(t)$ crosses these threshold values for the first time.
 490 These thresholds were determined by first calculating maximum distance,

$$\max \hat{D} = \max \hat{D}_{\tau,M}(t), \quad (3)$$

491 and mean pre-pandemic distance,

$$\hat{D}_{\text{mean}} = \frac{1}{N_{t<2020}} \sum_{t<2020} \hat{D}_{\tau,M}(t), \quad (4)$$

492 as a reference, and then dividing their ratios into K equal bins:

$$T_{\text{start}} = \hat{D}_{\text{mean}} \times \left(\frac{\max \hat{D}}{\hat{D}_{\text{mean}}} \right)^{(K-a)/K} \quad (5)$$

$$T_{\text{end}} = \hat{D}_{\text{mean}} \times \left(\frac{\max \hat{D}}{\hat{D}_{\text{mean}}} \right)^{a/K} \quad (6)$$

where a represents the truncation threshold. This allows us to discard the initial period during which the distance increases (from the introduction of intervention measures) and the final period during which the distance plateaus (as the system reaches an attractor). The fitting window is determined based on when the smoothed distance $\hat{D}_{\tau,M}(t)$ crosses these threshold values for the first time; then, we fit a linear regression to logged (unsmoothed) distances $\log D_{\tau,M}(t)$ using that window. Alongside the threshold R for the false nearest neighbors approach, we tested optimal choices for K and a values using simulations (Supplementary Text). We used $K = 19$ and $a = 2$ throughout the paper based on the simulation results.

Mathematical modeling

Throughout the paper, we use a series of mathematical models to illustrate the concept of pathogen resilience and to understand the determinants of pathogen resilience. In general, the intrinsic resilience for a given system is given by the largest real part of the eigenvalues of the linearized system at endemic equilibrium. Here, we focus on the SIRS model with demography (birth and death) and present the details of other models in Supplementary Text. The SIRS (Susceptible-Infected-Recovered-Susceptible) model is the simplest model that allows for waning of immunity, where recovered (immune) individuals are assumed to become fully susceptible after an average of $1/\delta$ time period. The dynamics of the SIRS model is described by the following set of differential equations:

$$\frac{dS}{dt} = \mu - \beta(t)SI - \mu S + \delta R \quad (7)$$

$$\frac{dI}{dt} = \beta(t)SI - (\gamma + \mu)I \quad (8)$$

$$\frac{dR}{dt} = \gamma I - (\delta + \mu)R \quad (9)$$

(10)

where μ represents the birth/death rate, $\beta(t)$ represents the time-varying transmission rate, and γ represents the recovery rate. The basic reproduction number $\mathcal{R}_0(t) = \beta(t)/(\gamma + \mu)$ is defined as the average number of secondary infections that a single infected individual would cause in a fully susceptible population at time t and measures the intrinsic transmissibility of a pathogen.

When we first introduced the idea of pathogen resilience (Figure 2), we imposed sinusoidal changes to the transmission rate to account for seasonal transmission:

$$\beta(t) = b_1(1 + \theta \cos(2\pi(t - \phi)))\alpha(t), \quad (11)$$

520 where b_1 represents the baseline transmission rate, θ represents the seasonal amplitude,
 521 and ϕ represents the seasonal offset term. Here, we also introduced an extra
 522 multiplicative term $\alpha(t)$ to account for the impact of pandemic perturbations, where
 523 $\alpha(t) < 1$ indicates transmission reduction. Figure 2A and 2B were generated assuming
 524 $b_1 = 3 \times (365/7 + 1/50)/\text{years}$, $\theta = 0.2$, $\phi = 0$, $\mu = 1/50/\text{years}$, $\gamma = 365/7/\text{years}$,
 525 and $\delta = 1/2/\text{years}$. In Figure 2A, we imposed a 50% transmission reduction for 6
 526 months from 2020:

$$\alpha(t) = \begin{cases} 0.5 & 2020 \leq t < 2020.5 \\ 1 & \text{otherwise} \end{cases} \quad (12)$$

527 In Figure 2B, we imposed a 50% transmission reduction for 6 months from 2020 and
 528 a permanent 10% reduction onward:

$$\alpha(t) = \begin{cases} 1 & t < 2020 \\ 0.5 & 2020 \leq t < 2020.5 \\ 0.9 & 2020.5 \leq t \end{cases} \quad (13)$$

529 In both scenarios, we simulated the SIRS model from the following initial conditions
 530 ($S(0) = 1/\mathcal{R}_0$, $I(0) = 1 \times 10^{-6}$, and $R(0) = 1 - S(0) - I(0)$) from 1900 until 2030.

531 To measure the empirical resilience of the SIRS model (Figure 2C and 2F), we
 532 computed the normalized distance between post-intervention susceptible and logged
 533 infected proportions and their corresponding unperturbed values at the same time:

$$\sqrt{\left(\frac{S(t) - S_{\text{unperturbed}}(t)}{\sigma_S}\right)^2 + \left(\frac{\log I(t) - \log I_{\text{unperturbed}}(t)}{\sigma_{\log I}}\right)^2}, \quad (14)$$

534 where σ_S and $\sigma_{\log I}$ represent the standard deviation in the unperturbed susceptible
 535 and logged infected proportions. The unperturbed values were obtained by simulating
 536 the same SIRS model without pandemic perturbations ($\alpha = 1$). We normalized
 537 the differences in susceptible and logged infected proportions to allow both quantities
 538 to equally contribute to the changes in distance from the attractor. We used logged
 539 prevalence, instead of absolute prevalence, in order to capture epidemic dynamics
 540 in deep troughs during the intervention period. In Supplementary Materials, we
 541 also compared how the degree of seasonal transmission affects empirical resilience
 542 by varying θ from 0 to 0.4; when we assumed no seasonality ($\theta = 0$), we did not
 543 normalize the distance because the standard deviation of pre-intervention dynamics
 544 are zero.

545 We used the SIRS model to understand how underlying epidemiological parameters
 546 affect pathogen resilience and link this relationship to underlying susceptible
 547 host dynamics. For the simple SIRS model without seasonal transmission ($\theta = 0$),
 548 the intrinsic resilience corresponds to

$$-\frac{\text{Re}(\lambda)}{2} = \frac{\delta + \beta I^* + \mu}{2}. \quad (15)$$

549 Here, I^* represents the prevalence at endemic equilibrium:

$$I^* = \frac{(\delta + \mu)(\beta - (\gamma + \mu))}{\beta(\delta + \gamma + \mu)}. \quad (16)$$

550 The susceptible replenishment rate is given by

$$S_{\text{replenish}} = \frac{\mu + \delta R}{S^*}, \quad (17)$$

551 where $S^* = 1/\mathcal{R}_0$ represents the equilibrium proportion of susceptible individuals.
552 We varied the basic reproduction number \mathcal{R}_0 between 1.1 to 6 and the average
553 duration of immunity $1/\delta$ between 2 to 4 years, and computed these two quantities.
554 In doing so, we fixed all other parameters: $\mu = 1/80/\text{years}$ and $\gamma = 365/7/\text{years}$.
555 When infection provides a life-long immunity ($\delta = 0$), the intrinsic resilience is
556 inversely proportional to the susceptible replenishment rate:

$$-\frac{\text{Re}(\lambda)}{2} = \frac{\mu}{2S^*} = \frac{S_{\text{replenish}}}{2}. \quad (18)$$

557 Finally, we used a seasonally unforced stochastic SIRS model without demog-
558 raphy to understand how pathogen resilience affects sensitivity of the system to
559 demographic stochasticity (see Supplementary Text for the details of the stochastic
560 SIRS model). By varying the basic reproduction number \mathcal{R}_0 between 2 to 20 and
561 the average duration of immunity $1/\delta$ between 1 to 40 years, we ran the the SIRS
562 model for 100 years and computed the epidemic amplitude, which we defined as
563 $(\max I - \min I)/(2\bar{I})$. Each simulation began from the equilibrium, and we trun-
564 cated initial 25 years before computing the epidemic amplitude. In doing so, we
565 assumed $\gamma = 365/7/\text{years}$ and fixed the population size to 1 billion to prevent any
566 fadeouts. We also considered using a seasonally forced stochastic SIRS model with-
567 out demography, assuming an amplitude of seasonal forcing of 0.04; in this case,
568 we computed the relative epidemic amplitude by comparing the deterministic and
569 stochastic trajectories (Supplementary Materials).

570 Data availability

571 All data and code are stored in a publicly available GitHub repository (<https://github.com/cobeylab/return-time>).
572

573 Funding

574 S.W.P. is a Peter and Carmen Lucia Buck Foundation Awardee of the Life Sciences
575 Research Foundation.

576 **Supplementary Text**

577 **Resilience of a stage-structured system.**

578 In Figure 2G–I, we used a more realistic, stage-structured model to illustrate how
 579 transient phenomena can cause the system to slow down. Specifically, we used the
 580 stage-structured RSV model proposed by [28], which assumes that subsequent rein-
 581 fections cause an individual to become less susceptible and transmissible than previ-
 582 ous infections. The model dynamics can be described as follows:

$$\frac{dM}{dt} = \mu - (\omega + \mu)M \quad (S1)$$

$$\frac{dS_0}{dt} = \omega M - (\lambda(t) + \mu)S_0 \quad (S2)$$

$$\frac{dI_1}{dt} = \lambda(t)S_0 - (\gamma_1 + \mu)I_1 \quad (S3)$$

$$\frac{dS_1}{dt} = \gamma_1 I_1 - (\sigma_1 \lambda(t) + \mu)S_1 \quad (S4)$$

$$\frac{dI_2}{dt} = \sigma_1 \lambda(t)S_1 - (\gamma_2 + \mu)I_2 \quad (S5)$$

$$\frac{dS_2}{dt} = \gamma_2 I_2 - (\sigma_2 \lambda(t) + \mu)S_2 \quad (S6)$$

$$\frac{dI_3}{dt} = \sigma_2 \lambda(t)S_2 - (\gamma_3 + \mu)I_3 \quad (S7)$$

$$\frac{dS_3}{dt} = \gamma_3 I_3 - (\sigma_3 \lambda(t) + \mu)S_3 + \gamma_4 I_4 \quad (S8)$$

$$\frac{dI_4}{dt} = \sigma_3 \lambda(t)S_3 - (\gamma_4 + \mu)I_4 \quad (S9)$$

(S10)

583 where M represents the proportion of individuals who are maternally immune; S_i
 584 represents the proportion of individuals who are susceptible after i prior infections; I_i
 585 represents the proportion of individuals who are currently (re)-infected with their i -th
 586 infection; μ represents the birth and death rates; $1/\omega$ represents the mean duration
 587 of maternal immunity; $1/\gamma_i$ represents the mean duration of infection; $\lambda(t)$ represents
 588 the force of infection; and σ_i represents the reduction in susceptibility for the i -th
 589 reinfection. The force of infection is modeled using a sinusoidal function:

$$\beta(t) = b_1(1 + \theta \cos(2\pi(t - \phi)))\alpha(t) \quad (S11)$$

$$\lambda(t) = \beta(I_1 + \rho_1 I_2 + \rho_2(I_3 + I_4)), \quad (S12)$$

590 where b_1 represents the baseline transmission rate; θ represents the seasonal ampli-
 591 tude; ϕ represents the seasonal offset term; $\alpha(t)$ represents the intervention effect;
 592 and ρ_i represents the impact of immunity on transmission reduction. We used the

593 following parameters to simulate the impact of interventions on epidemic dynam-
 594 ics [28]: $b_1 = 9 \times (365/10 + 1/80)/\text{years}$, $\theta = 0.2$, $\phi = -0.1$, $\omega = 365/112/\text{years}$,
 595 $\gamma_1 = 365/10/\text{years}$, $\gamma_2 = 365/7/\text{years}$, $\gamma_3 = 365/5/\text{years}$, $\sigma_1 = 0.76$, $\sigma_2 = 0.6$,
 596 $\sigma_3 = 0.4$, $\rho_1 = 0.75$, $\rho_2 = 0.51$, and $\mu = 1/80/\text{years}$. We assumed a 50% transmis-
 597 sion reduction for 6 months from 2020:

$$\alpha(t) = \begin{cases} 0.5 & 2020 \leq t < 2020.5 \\ 1 & \text{otherwise} \end{cases} \quad (\text{S13})$$

598 The model was simulated from 1900 to 2030 using the following initial conditions:
 599 $M = 0$, $S_0 = 1/\mathcal{R}_0 - I_1$, $I_1 = 1 \times 10^{-6}$, $S_1 = 1 - 1/\mathcal{R}_0$, $I_2 = 0$, $S_2 = 0$, $I_3 = 0$,
 600 $S_3 = 0$, and $I_4 = 0$. For the phase plane analysis (Figure 2H) and distance analysis
 601 (Figure 2I), we relied on the average susceptibility,

$$\bar{S} = S_0 + \sigma_1 S_1 + \sigma_2 S_2 + \sigma_3 S_3, \quad (\text{S14})$$

602 and total prevalence,

$$I_{\text{total}} = I_1 + I_2 + I_3 + I_4. \quad (\text{S15})$$

603 These quantities were used to compute the normalized distance from the attractor,
 604 as described in the main text.

605 Resilience of a multistrain system.

606 We used a simple two-strain model to show that a multistrain host-pathogen system
 607 that is coupled through cross immunity can be described by a single resilience value.
 608 The model dynamics can be described as follows [27]:

$$\frac{dS}{dt} = \mu - \mu S - (\lambda_1 + \lambda_2)S + \rho_1 R_1 + \rho_2 R_2 \quad (\text{S16})$$

$$\frac{dI_1}{dt} = \lambda_1 S - (\gamma_1 + \mu)I_1 \quad (\text{S17})$$

$$\frac{dI_2}{dt} = \lambda_2 S - (\gamma_2 + \mu)I_2 \quad (\text{S18})$$

$$\frac{dR_1}{dt} = \gamma_1 I_1 - \lambda_2 \epsilon_{21} R_1 - \rho_1 R_1 + \rho_2 R - \mu R_1 \quad (\text{S19})$$

$$\frac{dR_2}{dt} = \gamma_2 I_2 - \lambda_1 \epsilon_{12} R_2 - \rho_2 R_2 + \rho_1 R - \mu R_2 \quad (\text{S20})$$

$$\frac{dJ_1}{dt} = \lambda_1 \epsilon_{12} R_2 - (\gamma_1 + \mu)J_1 \quad (\text{S21})$$

$$\frac{dJ_2}{dt} = \lambda_2 \epsilon_{21} R_1 - (\gamma_2 + \mu)J_2 \quad (\text{S22})$$

$$\frac{dR}{dt} = \gamma_1 J_1 + \gamma_2 J_2 - \rho_1 R - \rho_2 R - \mu R \quad (\text{S23})$$

where S represents the proportion of individuals who are fully susceptible to infections by both strains; I_1 represents the proportion of individuals who are infected with strain 1 without prior immunity; I_2 represents the proportion of individuals who are infected with strain 2 without prior immunity; R_1 represents the proportion of individuals who are fully immune against strain 1 and partially susceptible to reinfection by strain 2; R_2 represents the proportion of individuals who are fully immune against strain 2 and partially susceptible to reinfection by strain 1; J_1 represents the proportion of individuals who are infected with strain 1 with prior immunity against strain 2; J_2 represents the proportion of individuals who are infected with strain 2 with prior immunity against strain 1; R represents the proportion of individuals who are immune to infections from both strains; μ represents the birth/death rate; λ_1 and λ_2 represent the force of infection from strains 1 and 2, respectively; ρ_1 and ρ_2 represent the waning immunity rate; γ_1 and γ_2 represent the recovery rate; ϵ_{12} and ϵ_{21} represent the susceptibility to reinfection with strains 2 and 1, respectively, given prior immunity from infection with strains 1 and 2, respectively. The force of infection is modeled as follows:

$$\beta_1 = b_1(1 + \theta_1 \sin(2\pi(t - \phi_1)))\alpha(t) \quad (\text{S24})$$

$$\beta_2 = b_2(1 + \theta_2 \sin(2\pi(t - \phi_2)))\alpha(t) \quad (\text{S25})$$

$$\lambda_1 = \beta_1(I_1 + J_1) \quad (\text{S26})$$

$$\lambda_2 = \beta_2(I_2 + J_2) \quad (\text{S27})$$

In Supplementary Figures S2–S4, we assumed the following parameters: $b_1 = 2 \times 52/\text{years}$, $b_2 = 4 \times 52/\text{years}$, $\phi_1 = \phi_2 = 0$, $\epsilon_{12} = 0.9$, $\epsilon_{21} = 0.5$, $\gamma_1 = \gamma_2 = 52/\text{years}$, $\rho_1 = \rho_2 = 1/\text{years}$, and $\mu = 1/70/\text{years}$. For all simulations, we assumed a 50% transmission reduction for 6 months from 2020:

$$\alpha(t) = \begin{cases} 0.5 & 2020 \leq t < 2020.5 \\ 1 & \text{otherwise} \end{cases} \quad (\text{S28})$$

The seasonal amplitude θ is varied from 0 to 0.4. All simulations were ran from 1900 to 2030 with following initial conditions: $S(0) = 1 - 2 \times 10^{-6}$, $I_1(0) = 1 \times 10^{-6}$, $I_2(0) = 1 \times 10^{-6}$, $R_1(0) = 0$, $R_2(0) = 0$, $J_1(0) = 0$, $J_2(0) = 0$, and $R(0) = 0$.

We considered three scenarios for measuring pathogen resilience: (1) we only have information about strain 1, (2) we only have information about strain 2, and (3) we are unable to distinguish between strains. In the first two scenarios (see panels A–C for strain 1 and panels D–F for strain 2), we considered the dynamics of average susceptibility for each strain and total prevalence:

$$\bar{S}_1 = S + \epsilon_{12}R_2 \quad (\text{S29})$$

$$\hat{I}_1 = I_1 + J_1 \quad (\text{S30})$$

$$\bar{S}_2 = S + \epsilon_{21}R_1 \quad (\text{S31})$$

$$\hat{I}_2 = I_2 + J_2 \quad (\text{S32})$$

637 In the third scenario (panels G–I), we considered the dynamics of total susceptible
638 and infected populations:

$$\hat{S} = S + R_2 + R_1 \quad (\text{S33})$$

$$\hat{I} = I_1 + J_1 + I_2 + J_2 \quad (\text{S34})$$

639 These quantities were used to compute the normalized distance from the attractor,
640 as described in the main text.

641 Estimating intrinsic resilience using mechanistic model

642 We tested whether we can reliably estimate the intrinsic resilience of a system by fit-
643 ting a mechanistic model. Specifically, we simulated case time series from stochastic
644 SIRS and two-strain models and fitted a simple, deterministic SIRS model using a
645 Bayesian framework.

646 We simulated the models in discrete time with a daily time step ($\Delta t = 1$),
647 incorporating demographic stochasticity:

$$\beta(t) = \mathcal{R}_0 \left(1 + \theta \cos \left(\frac{2\pi t}{364} \right) \right) \alpha(t)(1 - \exp(-\gamma)) \quad (\text{S35})$$

$$\text{FOI}(t) = \beta(t)I(t - \Delta t)/N \quad (\text{S36})$$

$$B(t) \sim \text{Poisson}(\mu N) \quad (\text{S37})$$

$$\Delta S(t) \sim \text{Binom}(S(t - \Delta t), 1 - \exp(-(\text{FOI}(t) + \mu)\Delta t)) \quad (\text{S38})$$

$$N_{SI}(t) \sim \text{Binom}\left(\Delta S(t), \frac{\text{FOI}(t)}{\text{FOI}(t) + \mu}\right) \quad (\text{S39})$$

$$\Delta I(t) \sim \text{Binom}(I(t - \Delta t), 1 - \exp(-(\gamma + \mu)\Delta t)) \quad (\text{S40})$$

$$N_{IR}(t) \sim \text{Binom}\left(\Delta I(t), \frac{\gamma}{\gamma + \mu}\right) \quad (\text{S41})$$

$$\Delta R(t) \sim \text{Binom}(R(t - \Delta t), 1 - \exp(-(\delta + \mu)\Delta t)) \quad (\text{S42})$$

$$N_{RS}(t) \sim \text{Binom}\left(\Delta R(t), \frac{\delta}{\delta + \mu}\right) \quad (\text{S43})$$

$$S(t) = S(t - \Delta t) + N_{RS}(t) + B(t) - \Delta S(t) \quad (\text{S44})$$

$$I(t) = I(t - \Delta t) + N_{SI}(t) - \Delta I(t) \quad (\text{S45})$$

$$R(t) = R(t - \Delta t) + N_{IR}(t) - \Delta R(t) \quad (\text{S46})$$

648 where FOI represent the force of infection; N_{ij} represent the number of individuals
649 moving from compartment i to j on a given day; and $B(t)$ represents the number
650 of new births. We simulated the model on a daily scale—assuming 364 days in a
651 year so that it can be evenly grouped into 52 weeks—with the following parameters:
652 $\mathcal{R}_0 = 3$, $\theta = 0.1$, $\gamma = 1/7/\text{days}$, $\delta = 1/(364 \times 2)/\text{days}$, $\mu = 1/(364 \times 50)/\text{days}$, and
653 $N = 1 \times 10^8$. The model was simulated from 1900 to 2030 assuming $S(0) = N/3$,

654 $I(0) = 100$, and $R(0) = N - S(0) - I(0)$. The observed incidence from the model
 655 was then simulated as follows:

$$C(t) = \text{Beta-Binom}(N_{SI}(t), \rho, k), \quad (\text{S47})$$

656 where ρ represents the reporting probability and k represents the overdispersion
 657 parameter of beta-binomial distribution. Here, we used the beta-binomial distribution
 658 to account for overdispersion in reporting. We assumed $\rho = 0.002$ (i.e., 0.2%
 659 probability) and $k = 1000$.

660 We used an analogous approach for the two-strain model:

$$\beta_1(t) = b_1 \left(1 + \theta_1 \cos \left(\frac{2\pi(t - \phi_1)}{364} \right) \right) \alpha(t) \quad (\text{S48})$$

$$\beta_2(t) = b_2 \left(1 + \theta_2 \cos \left(\frac{2\pi(t - \phi_2)}{364} \right) \right) \alpha(t) \quad (\text{S49})$$

$$\text{FOI}_1(t) = \beta_1(t)(I_1(t - \Delta t) + J_1(t - \Delta t))/N \quad (\text{S50})$$

$$\text{FOI}_2(t) = \beta_2(t)(I_2(t - \Delta t) + J_2(t - \Delta t))/N \quad (\text{S51})$$

$$B(t) \sim \text{Poisson}(\mu N) \quad (\text{S52})$$

$$\Delta S(t) \sim \text{Binom}(S(t - \Delta t), 1 - \exp(-(\text{FOI}_1(t) + \text{FOI}_2(t) + \mu)\Delta t)) \quad (\text{S53})$$

$$N_{SI_1}(t) \sim \text{Binom}\left(\Delta S(t), \frac{\text{FOI}_1(t)}{\text{FOI}_1(t) + \text{FOI}_2(t) + \mu}\right) \quad (\text{S54})$$

$$N_{SI_2}(t) \sim \text{Binom}\left(\Delta S(t), \frac{\text{FOI}_2(t)}{\text{FOI}_1(t) + \text{FOI}_2(t) + \mu}\right) \quad (\text{S55})$$

$$\Delta I_1(t) \sim \text{Binom}(I_1(t - \Delta t), 1 - \exp(-(\gamma_1 + \mu)\Delta t)) \quad (\text{S56})$$

$$N_{I_1 R_1}(t) \sim \text{Binom}\left(\Delta I_1(t), \frac{\gamma_1}{\gamma_1 + \mu}\right) \quad (\text{S57})$$

$$\Delta I_2(t) \sim \text{Binom}(I_2(t - \Delta t), 1 - \exp(-(\gamma_2 + \mu)\Delta t)) \quad (\text{S58})$$

$$N_{I_2 R_2}(t) \sim \text{Binom}\left(\Delta I_2(t), \frac{\gamma_2}{\gamma_2 + \mu}\right) \quad (\text{S59})$$

$$\Delta R_1(t) \sim \text{Binom}(R_1(t - \Delta t), 1 - \exp(-(\epsilon_{21}\text{FOI}_2(t) + \rho_1 + \mu)\Delta t)) \quad (\text{S60})$$

$$N_{R_1 S}(t) \sim \text{Binom}\left(\Delta R_1(t), \frac{\rho_1}{\epsilon_{21}\text{FOI}_2(t) + \rho_1 + \mu}\right) \quad (\text{S61})$$

$$N_{R_1 J_2}(t) \sim \text{Binom}\left(\Delta R_1(t), \frac{\epsilon_{21}\text{FOI}_2(t)}{\epsilon_{21}\text{FOI}_2(t) + \rho_1 + \mu}\right) \quad (\text{S62})$$

$$\Delta R_2(t) \sim \text{Binom}(R_2(t - \Delta t), 1 - \exp(-(\epsilon_{12}\text{FOI}_1(t) + \rho_2 + \mu)\Delta t)) \quad (\text{S63})$$

$$N_{R_2 S}(t) \sim \text{Binom}\left(\Delta R_2(t), \frac{\rho_2}{\epsilon_{12}\text{FOI}_1(t) + \rho_2 + \mu}\right) \quad (\text{S64})$$

$$N_{R_2 J_1}(t) \sim \text{Binom}\left(\Delta R_2(t), \frac{\epsilon_{12}\text{FOI}_1(t)}{\epsilon_{12}\text{FOI}_1(t) + \rho_2 + \mu}\right) \quad (\text{S65})$$

$$\Delta J_1(t) \sim \text{Binom}(J_1(t - \Delta t), 1 - \exp(-(\gamma_1 + \mu)\Delta t)) \quad (\text{S66})$$

$$N_{J_1R}(t) \sim \text{Binom} \left(\Delta J_1(t), \frac{\gamma_1}{\gamma_1 + \mu} \right) \quad (\text{S67})$$

$$\Delta J_2(t) \sim \text{Binom} (J_2(t - \Delta t), 1 - \exp(-(\gamma_2 + \mu)\Delta t)) \quad (\text{S68})$$

$$N_{J_2R}(t) \sim \text{Binom} \left(\Delta J_2(t), \frac{\gamma_2}{\gamma_2 + \mu} \right) \quad (\text{S69})$$

$$\Delta R(t) \sim \text{Binom} (R(t - \Delta t), 1 - \exp(-(\rho_1 + \rho_2 + \mu)\Delta t)) \quad (\text{S70})$$

$$N_{RR_1}(t) \sim \text{Binom} \left(\Delta R(t), \frac{\rho_1}{\rho_1 + \rho_2 + \mu} \right) \quad (\text{S71})$$

$$N_{RR_2}(t) \sim \text{Binom} \left(\Delta R(t), \frac{\rho_2}{\rho_1 + \rho_2 + \mu} \right) \quad (\text{S72})$$

$$S(t) = S(t - \Delta t) - \Delta S(t) + B(t) + N_{R_1S}(t) + N_{R_2S}(t) \quad (\text{S73})$$

$$I_1(t) = I_1(t - \Delta t) - \Delta I_1(t) + N_{SI_1}(t) \quad (\text{S74})$$

$$I_2(t) = I_2(t - \Delta t) - \Delta I_2(t) + N_{SI_2}(t) \quad (\text{S75})$$

$$R_1(t) = R_1(t - \Delta t) - \Delta R_1(t) + N_{I_1R_1}(t) + N_{RR_1}(t) \quad (\text{S76})$$

$$R_2(t) = R_2(t - \Delta t) - \Delta R_2(t) + N_{I_2R_2}(t) + N_{RR_2}(t) \quad (\text{S77})$$

$$J_1(t) = J_1(t - \Delta t) - \Delta J_1(t) + N_{R_2J_1}(t) \quad (\text{S78})$$

$$J_2(t) = J_2(t - \Delta t) - \Delta J_2(t) + N_{R_1J_2}(t) \quad (\text{S79})$$

$$R(t) = R(t - \Delta t) - \Delta R(t) + N_{J_1R}(t) + N_{J_2R}(t) \quad (\text{S80})$$

We simulated the model on a daily scale with previously estimated parameters for the RSV-HMPV interaction [27]: $b_1 = 1.7/\text{weeks}$, $b_2 = 1.95/\text{weeks}$, $\theta_1 = 0.4$, $\theta_2 = 0.3$, $\phi_1 = 0.005 \times 7/364$, $\phi_2 = 4.99 \times 7/364$, $\epsilon_{12} = 0.92$, $\epsilon_{21} = 0.45$, $\gamma_1 = 1/10/\text{days}$, $\gamma_2 = 1/10/\text{days}$, $\rho_1 = 1/364/\text{days}$, $\rho_2 = 1/364/\text{days}$, $\mu = 1/(70 \times 364)/\text{days}$, and $N = 1 \times 10^8$. The model was simulated from 1900 to 2030 assuming $S(0) = N - 200$, $I_1(0) = 100$, $I_2(0) = 100$, $R_1(0) = 0$, $R_2(0) = 0$, $J_1(0) = 0$, $J_2(0) = 0$, and $R(0) = 0$. The observed incidence for each strain is then simulated as follows:

$$C_1(t) = \text{Beta-Binom}(N_{SI_1}(t) + N_{R_2J_1}, \rho, k), \quad (\text{S81})$$

$$C_2(t) = \text{Beta-Binom}(N_{SI_2}(t) + N_{R_1J_2}, \rho, k), \quad (\text{S82})$$

where ρ represents the reporting probability and k represents the overdispersion parameter of beta-binomial distribution. We assumed $\rho = 0.002$ (i.e., 0.2% probability) and $k = 500$. We also considered the total incidence: $C_{\text{total}}(t) = C_1(t) + C_2(t)$.

For both models, we considered a more realistically shaped pandemic perturbation $\alpha(t)$ to challenge our ability to estimate the intervention effects. Thus, we assumed a 40% transmission reduction for 3 months from March 2020, followed by a 10% transmission reduction for 6 months, 20% transmission reduction for 3 months,

675 and a final return to normal levels:

$$\alpha(t) = \begin{cases} 1 & t < 2020.25 \\ 0.6 & 2020.25 \leq t < 2020.5 \\ 0.9 & 2020.5 \leq t < 2021 \\ 0.8 & 2021 \leq t < 2021.25 \\ 1 & 2021.25 \leq t \end{cases}. \quad (\text{S83})$$

676 For all simulations, we truncated the time series from the beginning of 2014 to the
677 end of 2023 and aggregate them into weekly cases.

678 To infer intrinsic resilience from time series, we fitted a simple discrete time,
679 deterministic SIRS model [4]:

$$\Delta t = 1 \text{ week} \quad (\text{S84})$$

$$\text{FOI}(t) = \beta(t)(I(t - \Delta t) + \omega)/N \quad (\text{S85})$$

$$\Delta S(t) = [1 - \exp(-(\text{FOI}(t) + \mu)\Delta t)] S(t - \Delta t) \quad (\text{S86})$$

$$N_{SI}(t) = \frac{\text{FOI}(t)\Delta S(t)}{\text{FOI}(t) + \mu} \quad (\text{S87})$$

$$\Delta I(t) = [1 - \exp(-(\gamma + \mu)\Delta t)] I(t - \Delta t) \quad (\text{S88})$$

$$N_{IR}(t) = \frac{\gamma \Delta I(t)}{\gamma + \mu} \quad (\text{S89})$$

$$\Delta R(t) = [1 - \exp(-(\nu + \mu)\Delta t)] R(t - \Delta t) \quad (\text{S90})$$

$$N_{RS}(t) = \frac{\nu \Delta R(t)}{\nu + \mu} \quad (\text{S91})$$

$$S(t) = S(t - \Delta t) + \mu S - \Delta S(t) + N_{RS}(t) \quad (\text{S92})$$

$$I(t) = I(t - \Delta t) - \Delta I(t) + N_{SI}(t) \quad (\text{S93})$$

$$R(t) = R(t - \Delta t) - \Delta R(t) + N_{IR}(t) \quad (\text{S94})$$

680 where we include an extra term ω to account for external infections. Although actual
681 simulations did not include any external infections, we found that including this term
682 generally helped with model convergence in previous analyses [4]. The transmission
683 rate was divided into a seasonal term $\beta_{\text{seas}}(t)$ (repeated every year) and intervention
684 term $\alpha(t)$, which were estimated jointly:

$$\beta(t) = \beta_{\text{seas}}(t)\alpha(t), \quad (\text{S95})$$

685 where $\alpha < 1$ corresponds to reduction in transmission due to intervention effects. To
686 constrain the smoothness of $\beta_{\text{seas}}(t)$, we imposed cyclic, random-walk priors:

$$\beta_{\text{seas}}(t) \sim \text{Normal}(\beta_{\text{seas}}(t - 1), \sigma) \quad t = 2 \dots 52 \quad (\text{S96})$$

$$\beta_{\text{seas}}(1) \sim \text{Normal}(\beta_{\text{seas}}(52), \sigma) \quad (\text{S97})$$

687 [SWP: I noticed that I forgot to put a prior on σ so need to re-do this but won't
 688 change the results.] We fixed $\alpha(t) = 1$ for all $t < 2020$ and estimate α assuming a
 689 normal prior:

$$\alpha \sim \text{Normal}(1, 0.25). \quad (\text{S98})$$

690 We assumed weakly informative priors on ω and ν :

$$\omega \sim \text{Normal}(0, 200) \quad (\text{S99})$$

$$\nu \sim \text{Normal}(104, 26) \quad (\text{S100})$$

691 We assumed that the true birth/death rates, population sizes, and recovery rates are
 692 known. We note, however, that assuming $\gamma = 1/\text{week}$ actually corresponds to a mean
 693 simulated infectious period of 1.6 weeks, which is much longer than the true value;
 694 this approximation allows us to test whether we can still robustly estimate the in-
 695 trinsic resilience given parameter mis-specification. Initial conditions were estimated
 696 with following priors:

$$S(0) = Ns(0) \quad (\text{S101})$$

$$I(0) = Ni(0) \quad (\text{S102})$$

$$s(0) \sim \text{Uniform}(0, 1) \quad (\text{S103})$$

$$i(0) \sim \text{Half-Normal}(0, 0.001) \quad (\text{S104})$$

697 Finally, the observation model was specified as follows:

$$\text{Cases}(t) \sim \text{Negative-Binomial}(\rho N_{SI}(t), \phi) \quad (\text{S105})$$

$$\rho \sim \text{Half-Normal}(0, 0.02) \quad (\text{S106})$$

$$\phi \sim \text{Half-Normal}(0, 10) \quad (\text{S107})$$

698 where ρ represents the reporting probability and ϕ represents the negative binomial
 699 overdispersion parameter.

700 The model was fitted to four separate time series: (1) incidence time series from
 701 the SIRS model, (2) incidence time series for strain 1 from the two-strain model,
 702 (3) incidence time series for strain 2 from the two-strain model, and (4) combined
 703 incidence time series for strains 1 and 2 from the two-strain model. The model was
 704 fitted using rstan [37, 38]. The resulting posterior distribution was used to calculate
 705 the intrinsic resilience of the seasonally unforced system with the same parameters;
 706 eigenvalues of the discrete-time SIR model were computed by numerically finding
 707 the equilibrium and calculating the Jacobian matrix.

708 **Validations for window-selection criteria**

709 We used stochastic SIRS simulations to identify optimal parameters for the window-
 710 selection criteria that we used for the linear regression for estimating empirical re-
 711 silience. For each simulation, we began by generating a random perturbation $\alpha(t)$

712 from a random set of parameters. First, we drew the duration of perturbation τ_{np}_i
 713 from a uniform distribution between 1 and 2 years. Then, we drew independent
 714 normal variables z_i of length $\lfloor 364\tau_{\text{np}}_i \rfloor$ with a standard deviation of 0.02 and took a
 715 reverse cumulative sum to obtain a realistic shape for the perturbation:

$$x_n = 1 + \sum_{i=n}^{\lfloor 364\tau_{\text{np}}_i \rfloor} z_i, \quad n = 1, \dots, \lfloor 364\tau_{\text{np}}_i \rfloor. \quad (\text{S108})$$

716 We repeated this random generation process until less than 10% of x_n exceeds 1—
 717 this was done to prevent the perturbation $\alpha(t)$ stays below 1 (and therefore reduce
 718 transmission) for the most part. Then, we set any values that are above 1 or below 0
 719 as 1 and 0, respectively. Then, we randomly drew the minimum transmission during
 720 perturbation α_{\min} from a uniform distribution between 0.5 and 0.7 and scale x_n to
 721 have a minimum of α_{\min} :

$$x_{\text{scale},n} = \alpha_{\min} + (1 - \alpha_{\min}) \times \frac{x_n - \min x_n}{1 - \min x_n}. \quad (\text{S109})$$

722 This allowed us to simulate a realistically shaped perturbation:

$$\alpha(t) = \begin{cases} 1 & t < 2020 \\ x_{\text{scale},364(t-2020)} & 2020 \leq t < 2020 + \tau_{\text{np}}_i \\ 1 & \tau_{\text{np}}_i \leq t \end{cases}. \quad (\text{S110})$$

723 Given this perturbation function, we draw \mathcal{R}_0 from a uniform distribution between
 724 1.5 and 4 and the mean duration of immunity $1/\delta$ from a uniform distribution be-
 725 tween 1 and 4. Then, we simulate the stochastic SIRS model from $S(0) = 10^8/\mathcal{R}_0$
 726 and $I(0) = 100$ from 1990 to 2025 and truncate the time series to 2014–2025; if the
 727 epidemic becomes extinct before the end of simulation, we discard that simulation
 728 and start over from the perturbation generation step.

729 For each epidemic simulation, we computed the empirical resilience by varying
 730 the threshold R for the nearest neighbor approach from 4 to 14 with increments of
 731 2, the number of divisions K for the window selection between 8 and 25, and the
 732 truncation threshold a for the window selection between 1 to 3; this was done for all
 733 possible combinations of R , K , and a . We also compared this with the naive approach
 734 that uses the entire distance-from-attractor time series, starting from the maximum
 735 distance to the end of the time series. We repeated this procedure 500 times and
 736 quantified the correlation between empirical and intrinsic resilience estimates across
 737 two approaches.

Supplementary Figures

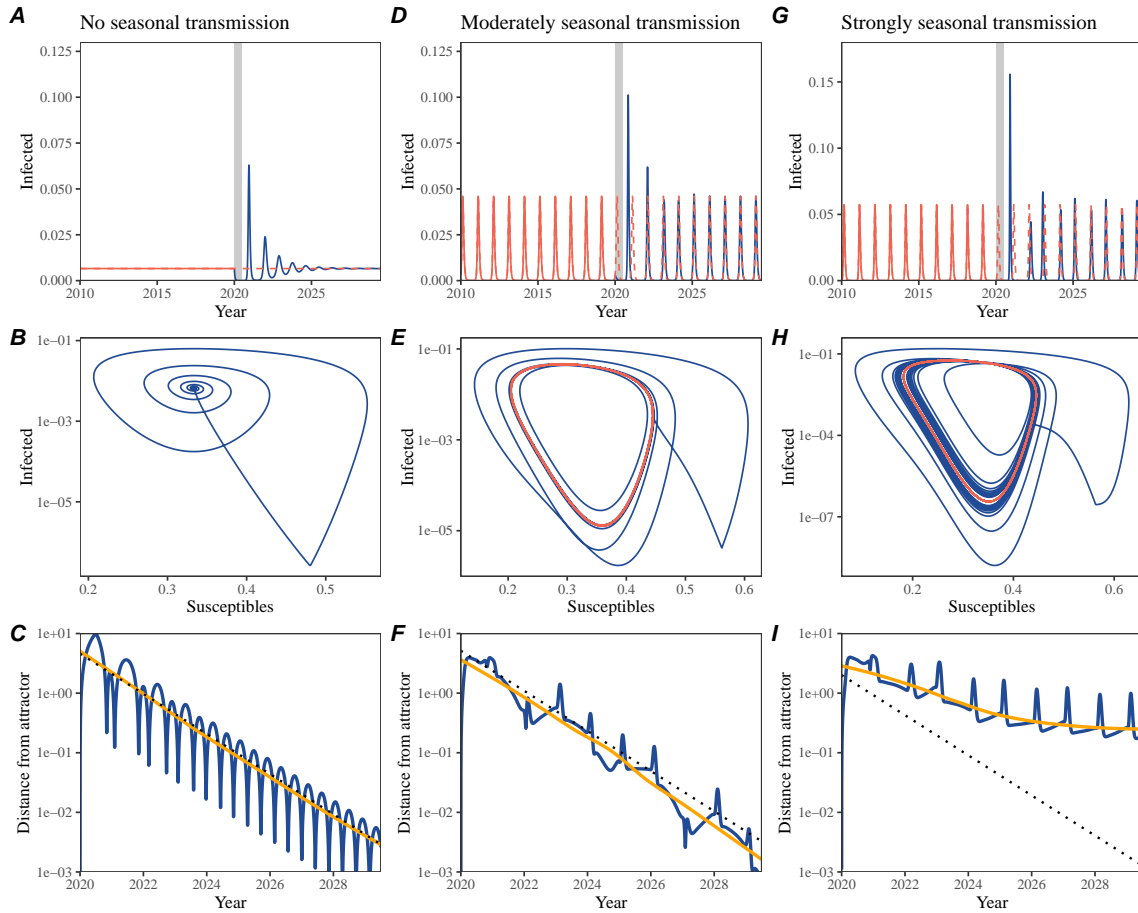


Figure S1: Impact of seasonal transmission on pathogen resilience. (A, D, G) Simulated epidemic trajectories using the SIRS model without seasonal forcing (A), with seasonal forcing of amplitude of 0.2 (D), and with seasonal forcing of amplitude of 0.4 (G). Red and blue solid lines represent epidemic dynamics before and after interventions are introduced, respectively. Red dashed lines represent counterfactual epidemic dynamics in the absence of interventions. Gray regions indicate the duration of interventions. (B, E, H) Phase plane representation of the time series in panels A, D, and G alongside the corresponding susceptible host dynamics. Red and blue solid lines represent epidemic trajectories on an SI phase plane before and after interventions are introduced, respectively. (C, F, I) Changes in logged distance from the attractor over time. Blue lines represent the logged distance from the attractor. Orange lines represent the locally estimated scatterplot smoothing (LOESS) fits to the logged distance from the attractor. Dotted lines show the intrinsic resilience of the seasonally unforced system.

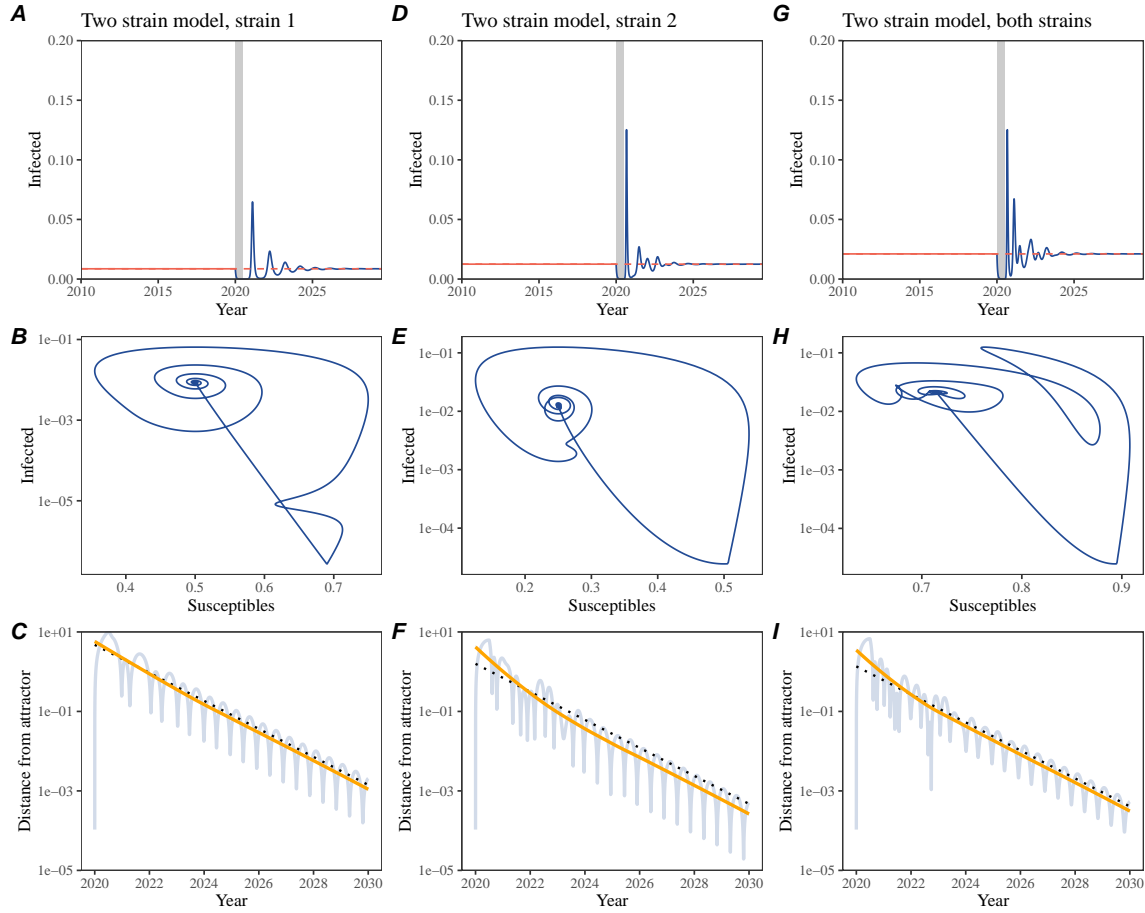


Figure S2: A simple method to measure pathogen resilience following pandemic perturbations for a two-strain system without seasonal forcing. (A, D, G) Simulated epidemic trajectories using a multi-strain system without seasonal forcing. Red and blue solid lines represent epidemic dynamics before and after interventions are introduced, respectively. Red dashed lines represent counterfactual epidemic dynamics in the absence of interventions. Gray regions indicate the duration of interventions. (B, E, H) Phase plane representation of the time series in panels A, D, and G alongside the corresponding susceptible host dynamics. Blue solid lines represent epidemic trajectories on an SI phase plane before and after interventions are introduced, respectively. (C, F, I) Changes in logged distance from the attractor over time. Blue lines represent the logged distance from the attractor. Orange lines represent the locally estimated scatterplot smoothing (LOESS) fits to the logged distance from the attractor. Dotted lines show the intrinsic resilience of the seasonally unforced system.

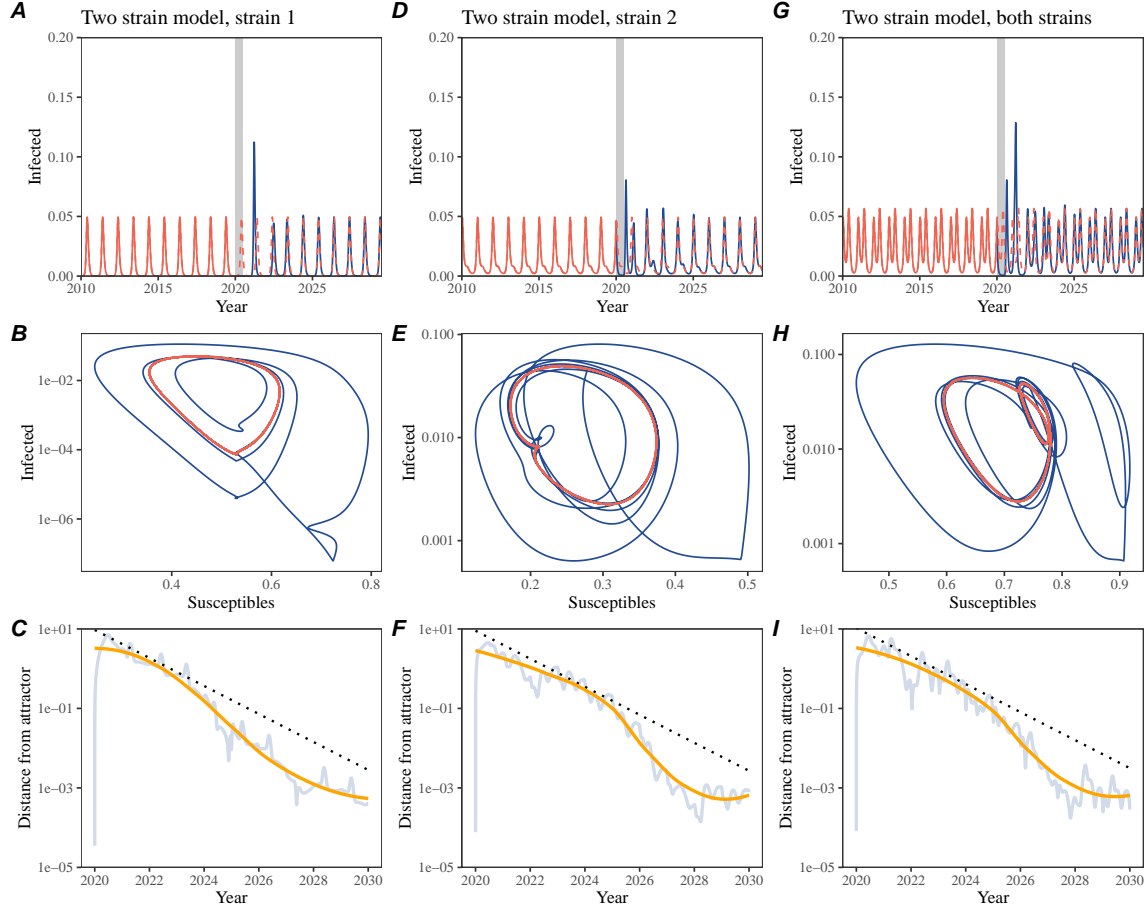


Figure S3: A simple method to measure pathogen resilience following pandemic perturbations for a two-strain system with seasonal forcing. (A, D, G) Simulated epidemic trajectories using a two-strain system with seasonal forcing (amplitude of 0.2). In this model, two strains compete through cross immunity. Red and blue solid lines represent epidemic dynamics before and after interventions are introduced, respectively. Red dashed lines represent counterfactual epidemic dynamics in the absence of interventions. Gray regions indicate the duration of interventions. (B, E, H) Phase plane representation of the time series in panels A, D, and G alongside the corresponding susceptible host dynamics. Red and blue solid lines represent epidemic trajectories on an SI phase plane before and after interventions are introduced, respectively. (C, F, I) Changes in logged distance from the attractor over time. Blue lines represent the logged distance from the attractor. Orange lines represent the locally estimated scatterplot smoothing (LOESS) fits to the logged distance from the attractor. Dotted lines show the intrinsic resilience of the seasonally unforced system.

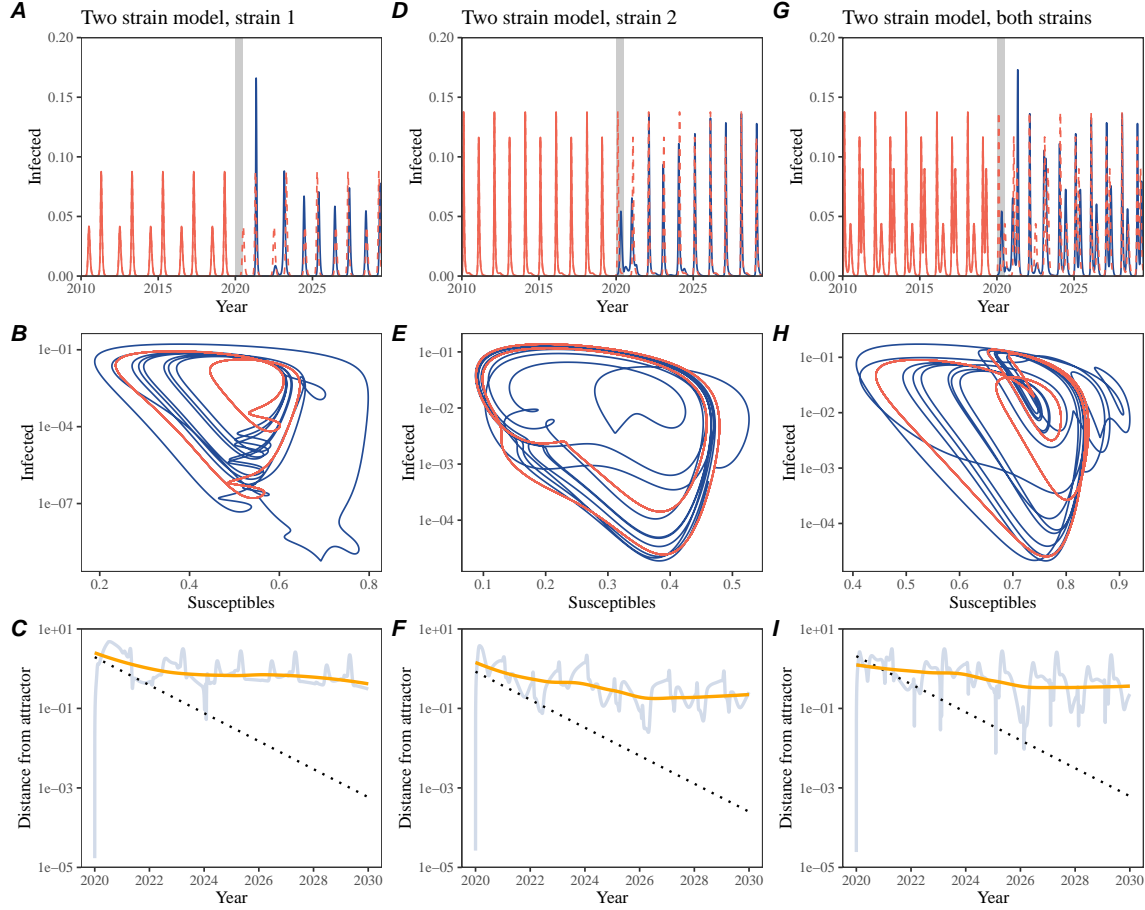


Figure S4: A simple method to measure pathogen resilience following pandemic perturbations for a multi-strain system with strong seasonal forcing. (A, D, G) Simulated epidemic trajectories using a multi-strain system with seasonal forcing (amplitude of 0.4). In this model, two strains compete through cross immunity. Red and blue solid lines represent epidemic dynamics before and after interventions are introduced, respectively. Red dashed lines represent counterfactual epidemic dynamics in the absence of interventions. Gray regions indicate the duration of interventions. (B, E, H) Phase plane representation of the time series in panels A, D, and G alongside the corresponding susceptible host dynamics. Red and blue solid lines represent epidemic trajectories on an SI phase plane before and after interventions are introduced, respectively. (C, F, I) Changes in logged distance from the attractor over time. Blue lines represent the logged distance from the attractor. Orange lines represent the locally estimated scatterplot smoothing (LOESS) fits to the logged distance from the attractor. Dotted lines show the intrinsic resilience of the seasonally unforced system.

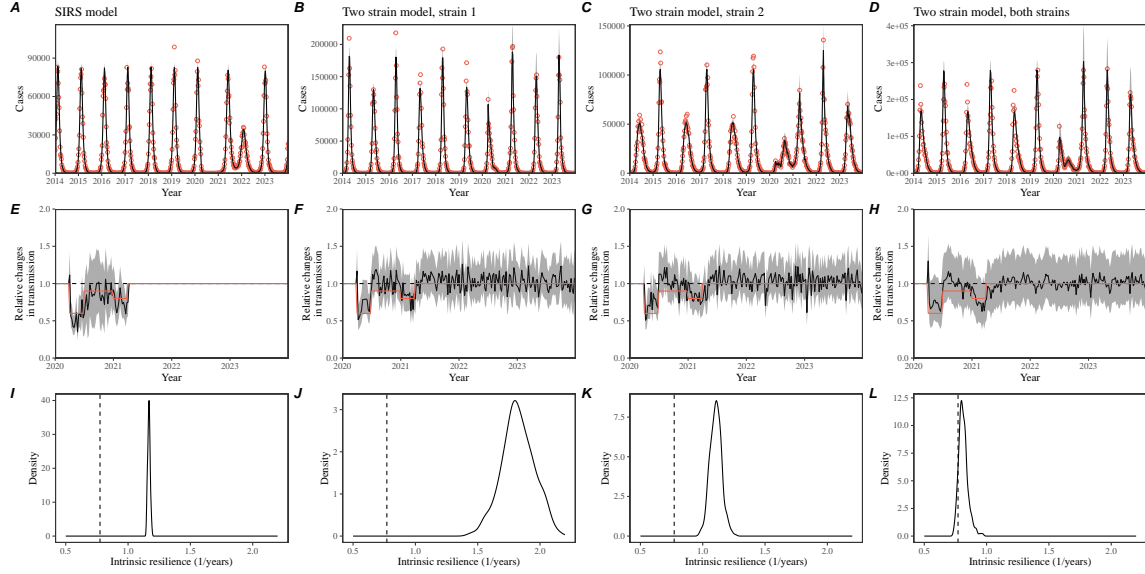


Figure S5: Mechanistic model fits to simulated data and inferred intrinsic resilience. We simulated discrete time, stochastic epidemic trajectories using seasonally forced SIRS model (A,E,I) and seasonally forced two-strain model (B–D, F–H, and J–L) and tested whether we can estimate the intrinsic resilience of the seasonally unforced versions of the model by fitting a mechanistic model (Supplementary Text). We fitted the same discrete time, deterministic SIRS model across all four scenarios. (A–D) Simulated case time series from corresponding models shown in the title (red) and SIRS model fits (black). (E–H) Assumed changes in transmission due to pandemic perturbations (red) and estimated time-varying relative transmission rates for the perturbation impact from the SIRS model fits (black). Solid lines and shaded regions represent fitted posterior median and 95% credible intervals. (I–L) True intrinsic resilience of the seasonally unforced system (vertical lines) and the posterior distribution of the inferred intrinsic resilience from the SIRS model (density plots).

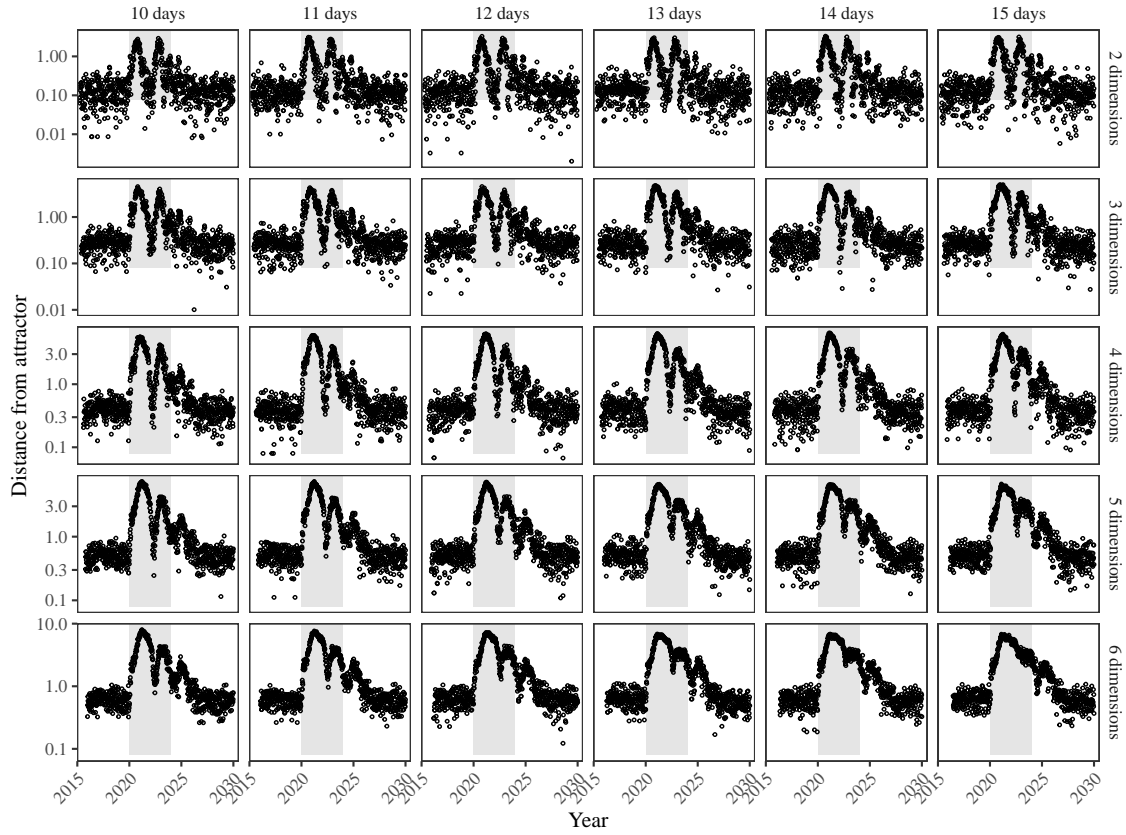


Figure S6: Sensitivity of the distance from the attractor to choices about embedding lags and dimensions. Sensitivity analysis for the distance-from-attractor time series shown in Figure 3E in the main text by varying the embedding lag between 10–15 days and embedding dimensions between 2–6 dimensions. [SWP: You said: “Did you do sensitivity analyses with other systems or just this one? I think we’ll probably need to do it with several systems”. I think it’s OK to just do this because we’re just trying to show qualitatively that longer lags and higher dimensions smooth things out. We also explore resilience of other models in other figures.]

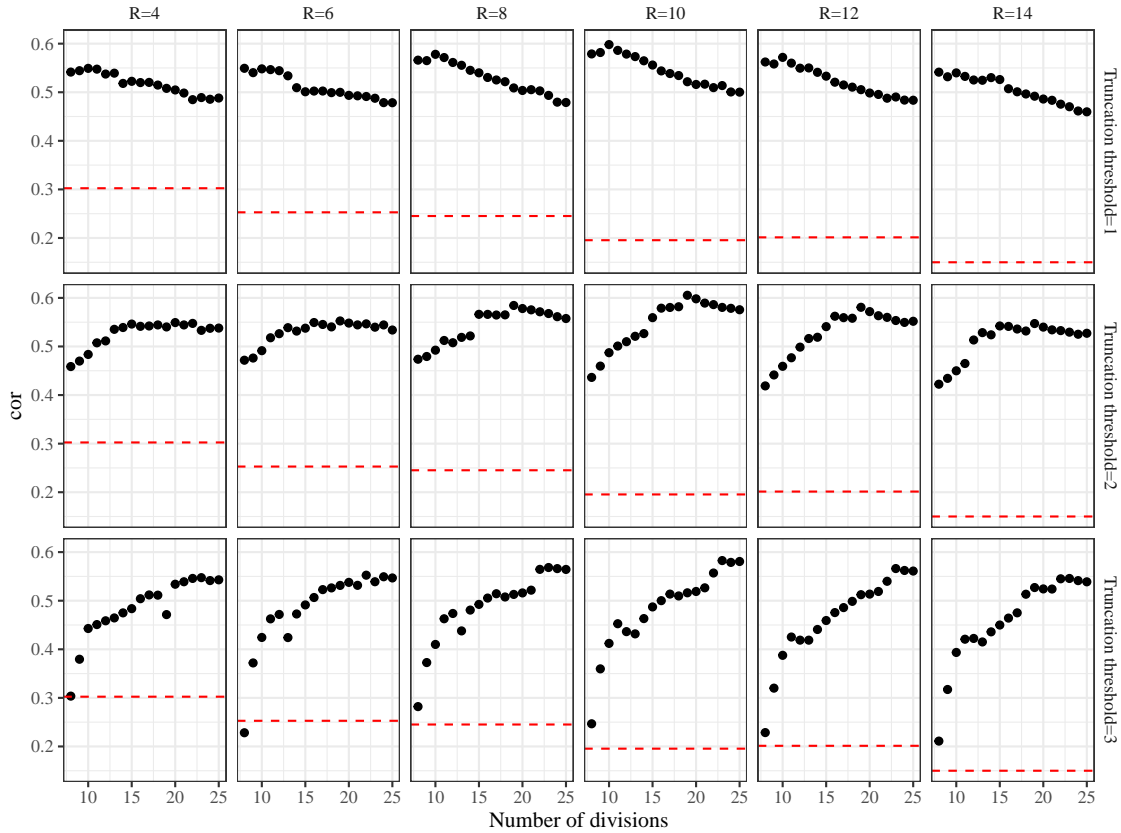


Figure S7: Impact of fitting window selection on the estimation of empirical resilience. We simulated 500 epidemics of a stochastic SIRS model with randomly drawn parameters and randomly generated pandemic perturbations (Supplementary Text). For each simulation, we varied the false nearest neighbor threshold R for reconstructing the empirical attractor as well as the parameters for regression window selection (i.e., the truncation threshold a and the the number of divisions K). Each point represents the resulting correlation coefficient between empirical and intrinsic resilience estimates for a given scenario. Dashed lines represent the correlation coefficient between empirical and intrinsic resilience estimates for the naive approach that fits a linear regression on a log scale, starting from the maximum distance until the end of the time series.

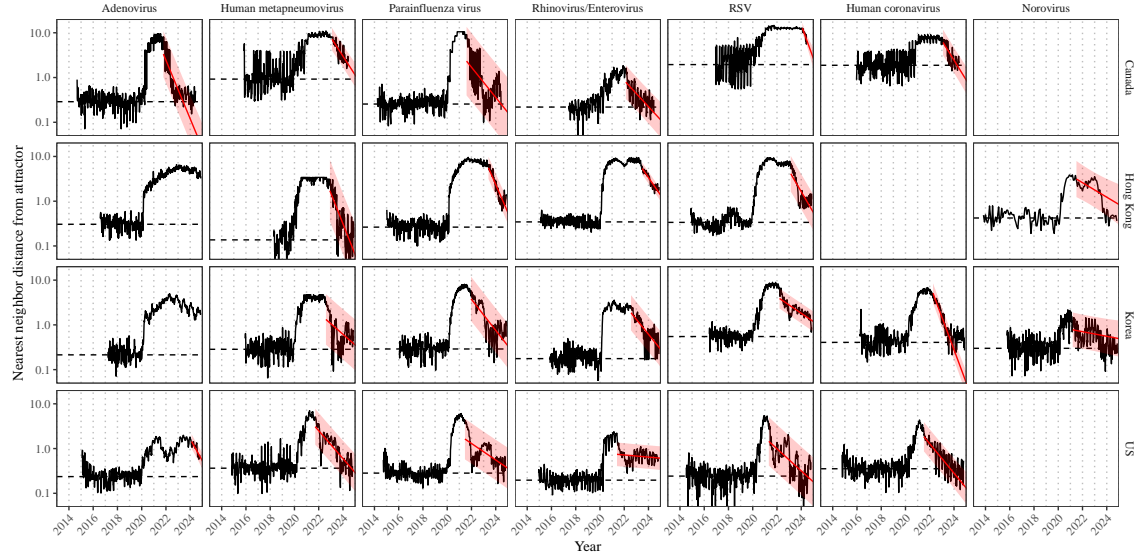


Figure S8: Estimated time series of distance from the attractor for each pathogen and corresponding linear regression fits using automated window selection criterion across Canada, Hong Kong, Korea, and the US. Black lines represent the estimated distance from the attractor. Red lines and shaded regions represent the linear regression fits and corresponding 95% confidence intervals. Dashed lines represent the average of the pre-pandemic nearest neighbor distances.

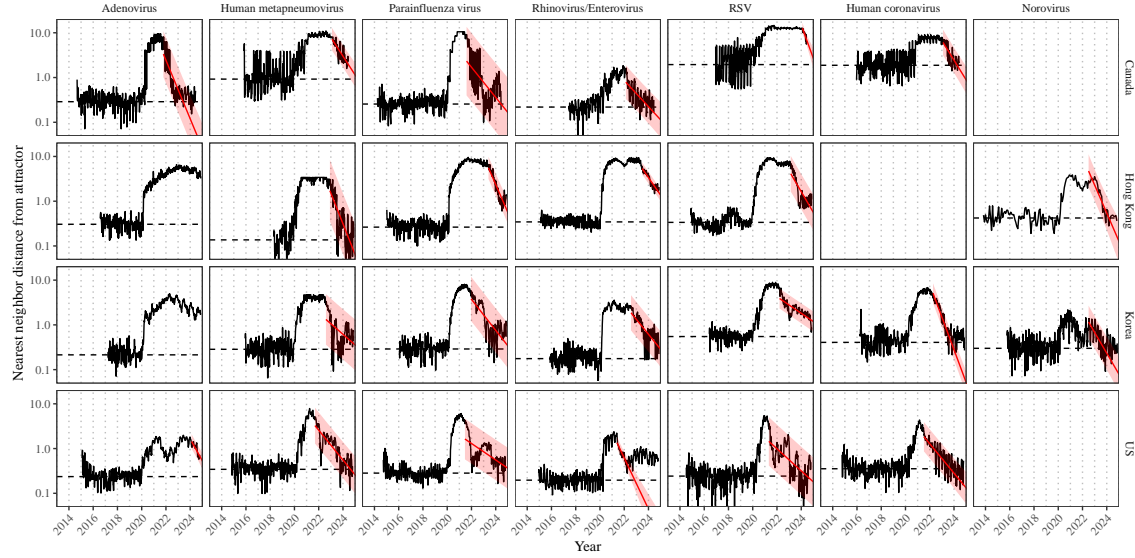


Figure S9: Estimated time series of distance from the attractor for each pathogen and corresponding linear regression fits across Canada, Hong Kong, Korea, and the US, including ad-hoc regression window selection. We used ad-hoc regression windows for norovirus in Hong Kong and Korea and Rhinovirus/Enterovirus in the US. Black lines represent the estimated distance from the attractor. Red lines and shaded regions represent the linear regression fits and corresponding 95% confidence intervals. Dashed lines represent the average of the pre-pandemic nearest neighbor distances.

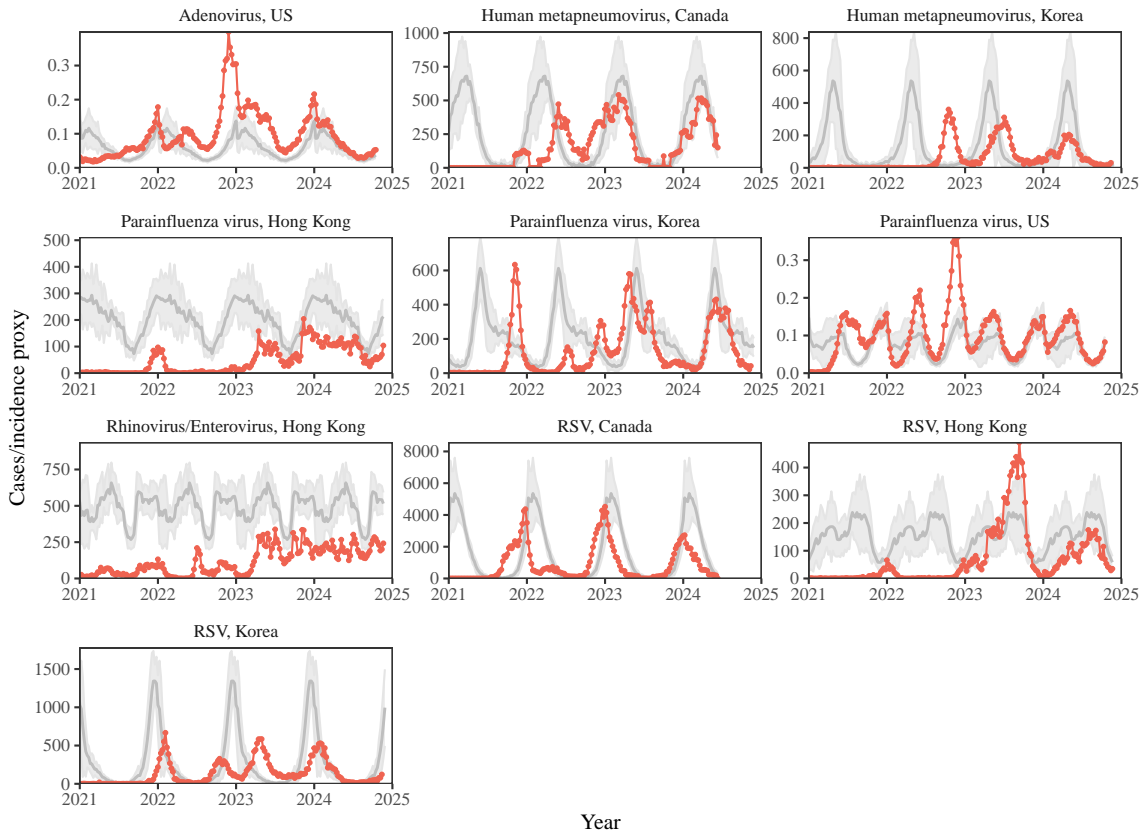


Figure S10: Observed dynamics for pathogen that are predicted to return after the end of 2024. Red points and lines represent data before 2020. Gray lines and shaded regions represent the mean seasonal patterns and corresponding 95% confidence intervals around the mean, previously shown in Figure 1.

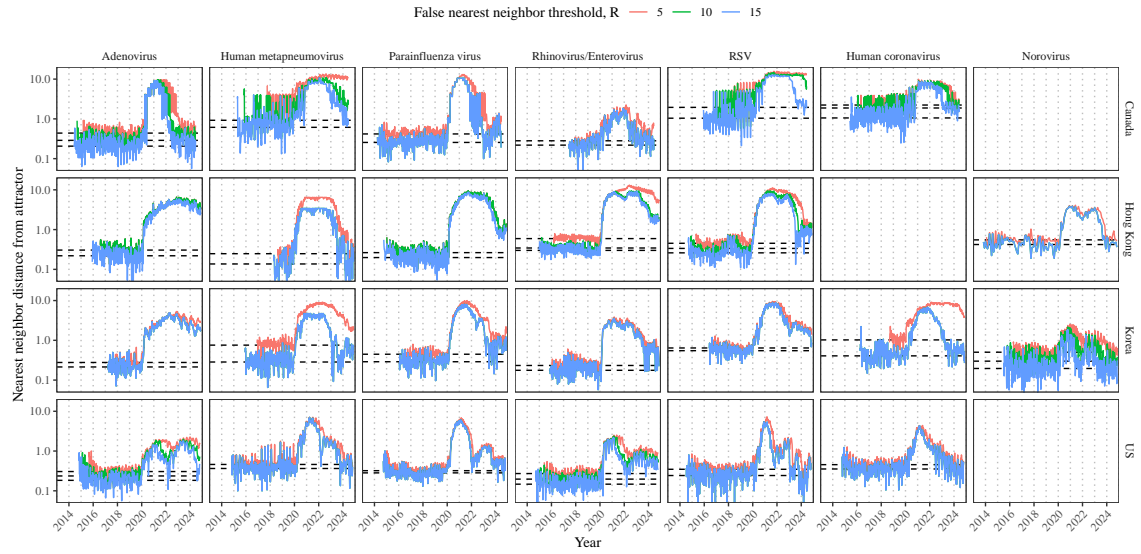


Figure S11: Estimated time series of distance from the attractor for each pathogen across different choices about false nearest neighbor threshold values. Using higher threshold values for the false nearest neighbor approach gives lower embedding dimensions. Colored lines represent the estimated distance from the attractor for different threshold values.

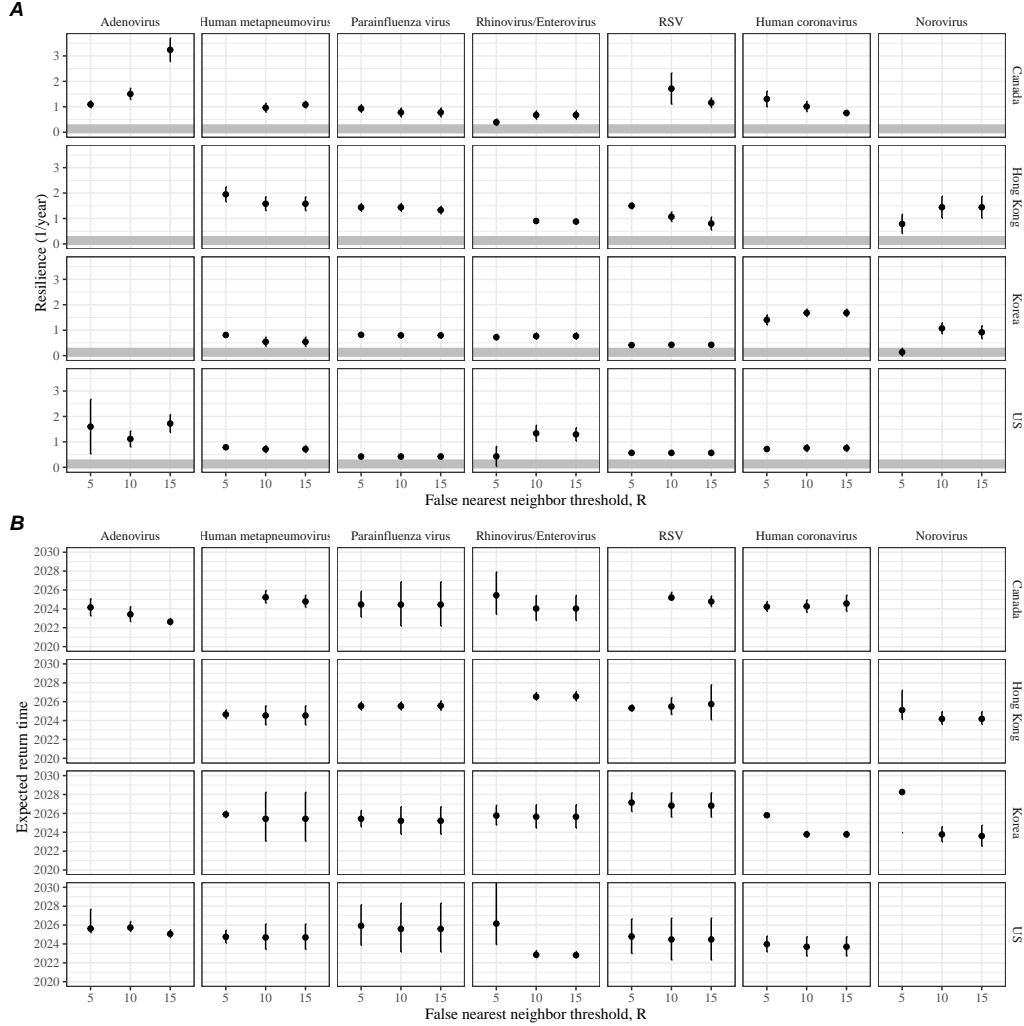


Figure S12: Summary of resilience estimates and predictions for return time across different choices about false nearest neighbor threshold values. The automated window selection method was used for all scenarios to estimate pathogen resilience, except for norovirus in Hong Kong and Korea and Rhinovirus/Enterovirus in the US. We used the same ad-hoc regression windows for norovirus in Hong Kong and Korea and Rhinovirus/Enterovirus in the US as we did in the main analysis. (A) Estimated pathogen resilience. The gray horizontal line represents the intrinsic resilience of pre-vaccination measles dynamics. (B) Predicted timing of when each pathogen will return to their pre-pandemic cycles. The dashed line in panel B indicates the end of 2024. Error bars represent 95% confidence intervals.

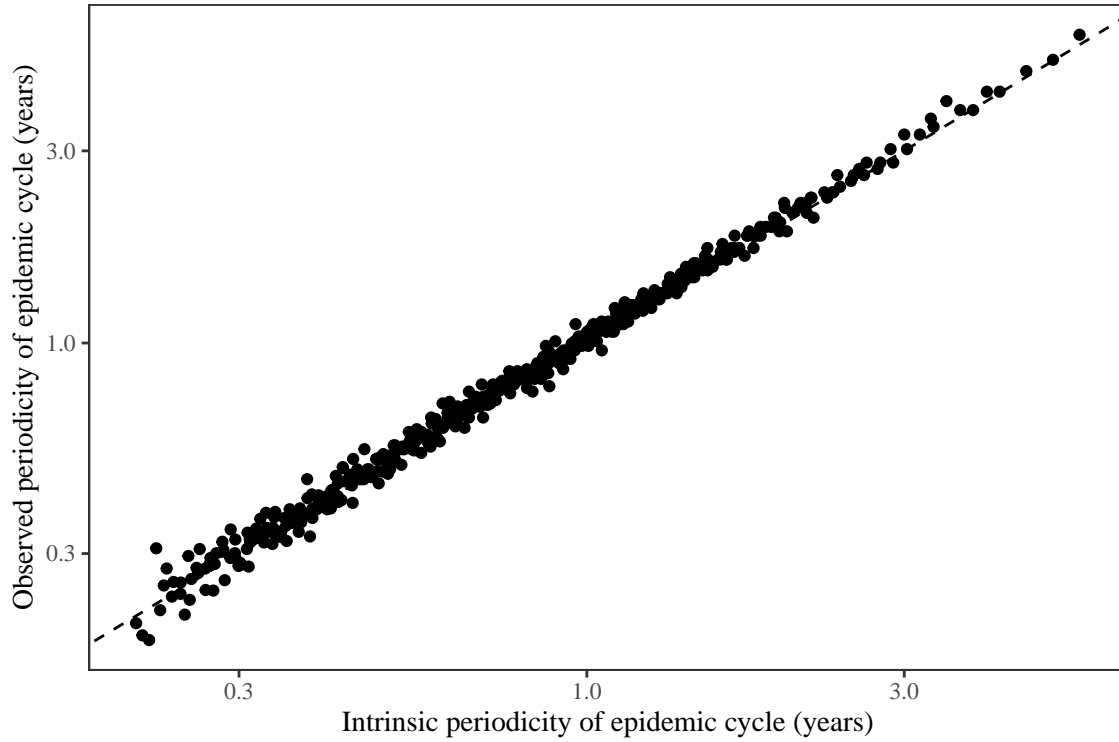


Figure S13: Comparison between the observed and intrinsic periodicity of the epidemic cycle of the seasonally unforced SIRS model. The observed periodicity of the epidemic corresponds to the periodicity at which maximum spectral density occurs. The intrinsic periodicity of the epidemic corresponds to $2\pi/\text{Im}(\lambda)$, where $\text{Im}(\lambda)$ is the imaginary part of the eigenvalue.

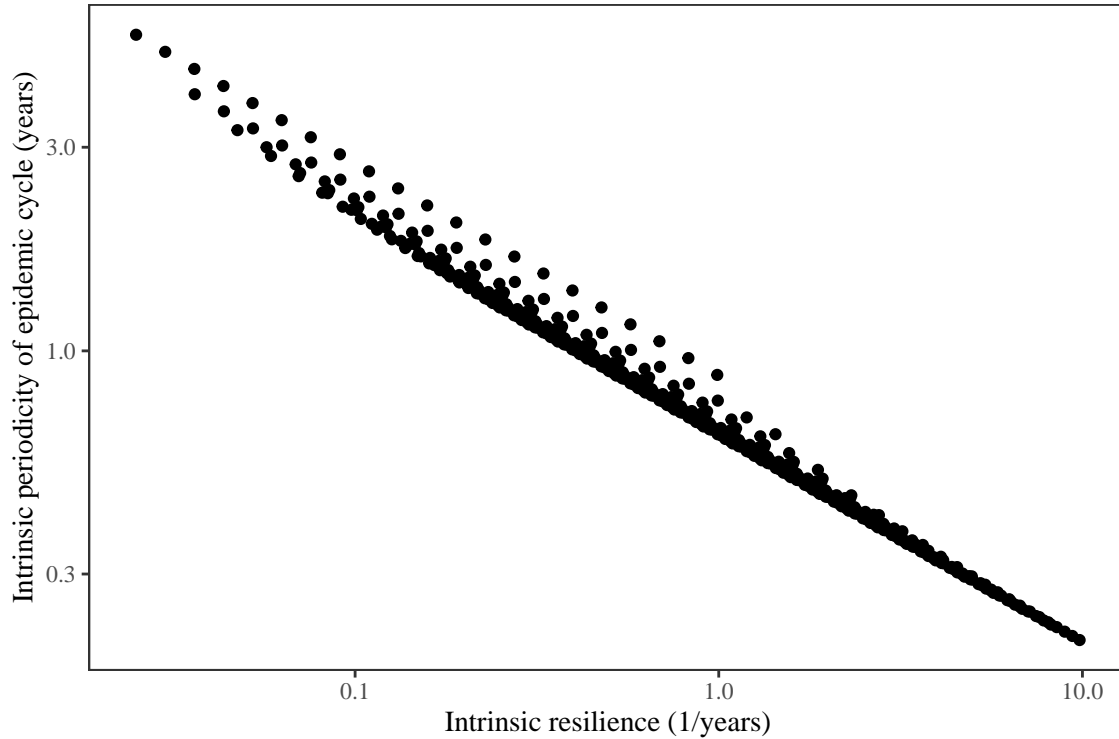


Figure S14: **Comparison between the intrinsic resilience and periodicity of the epidemic cycle of the seasonally unforced SIRS model.** The intrinsic resilience of the epidemic corresponds to the negative of the real value of the eigenvalue $-\text{Re}(\lambda)$. The intrinsic periodicity of the epidemic corresponds to $2\pi/\text{Im}(\lambda)$, where $\text{Im}(\lambda)$ is the imaginary part of the eigenvalue.

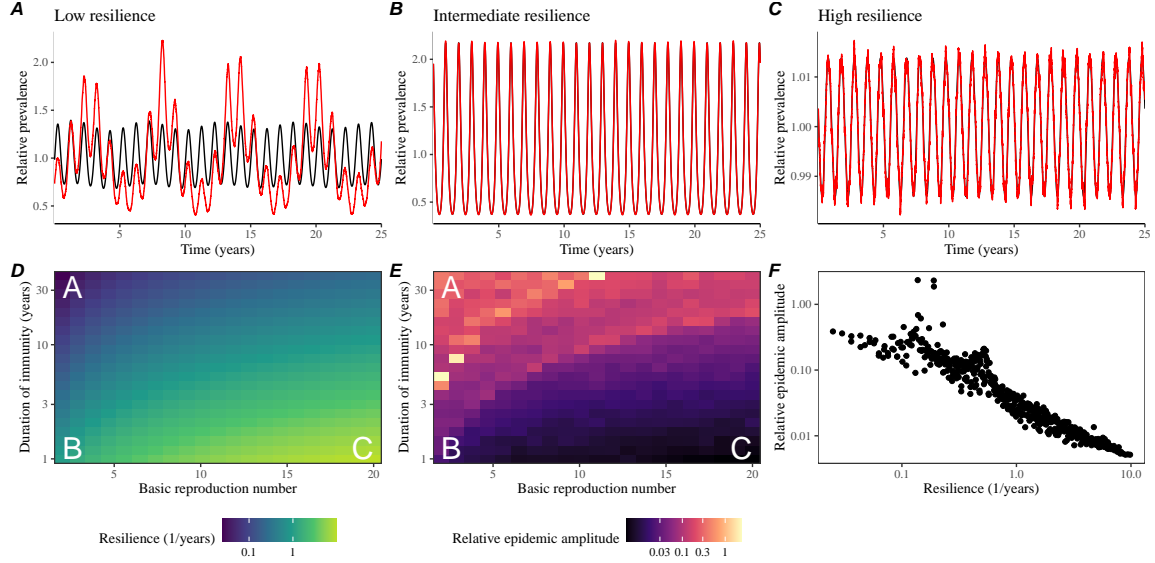


Figure S15: Linking resilience of a host-pathogen system to its sensitivity to stochastic perturbations for the seasonally forced SIRS model. (A–C) Epidemic trajectories of a stochastic SIRS model across three different resilience values: low, intermediate, and high. The relative prevalence was calculated by dividing infection prevalence by its mean value. (D) The heat map represents the intrinsic resilience of the seasonally unforced system as a function of the basic reproduction number \mathcal{R}_0 and the duration of immunity. (E) The heat map represents the relative epidemic amplitude as a function of the basic reproduction number \mathcal{R}_0 and the duration of immunity. To calculate the relative epidemic amplitude, we first take the relative difference in infection prevalence between stochastic and deterministic trajectories: $\epsilon = (I_{\text{stoch}} - I_{\text{det}})/I_{\text{det}}$. Then, we calculate the difference between maximum and minimum of the relative difference and divide by half: $(\max \epsilon - \min \epsilon)/2$. (F) The relationship between pathogen resilience and relative epidemic amplitude.

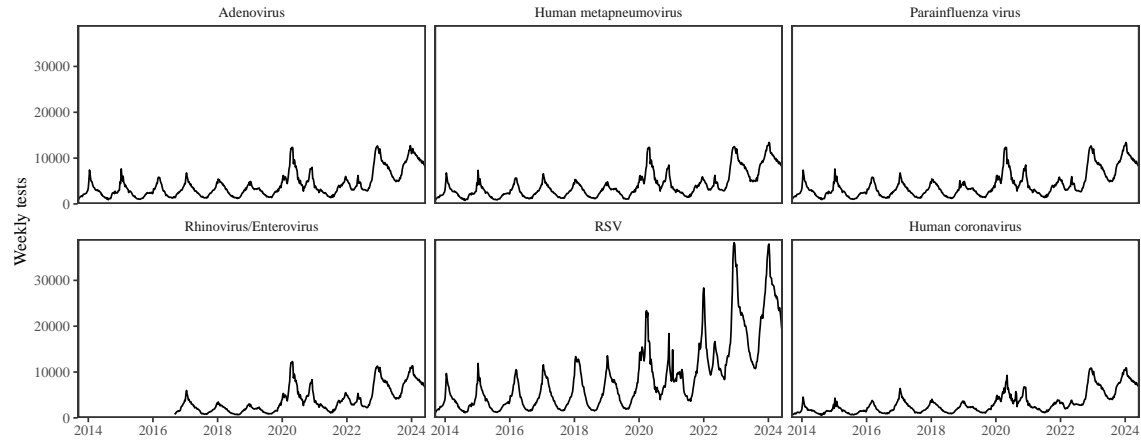


Figure S16: Testing patterns for respiratory pathogens in Canada.

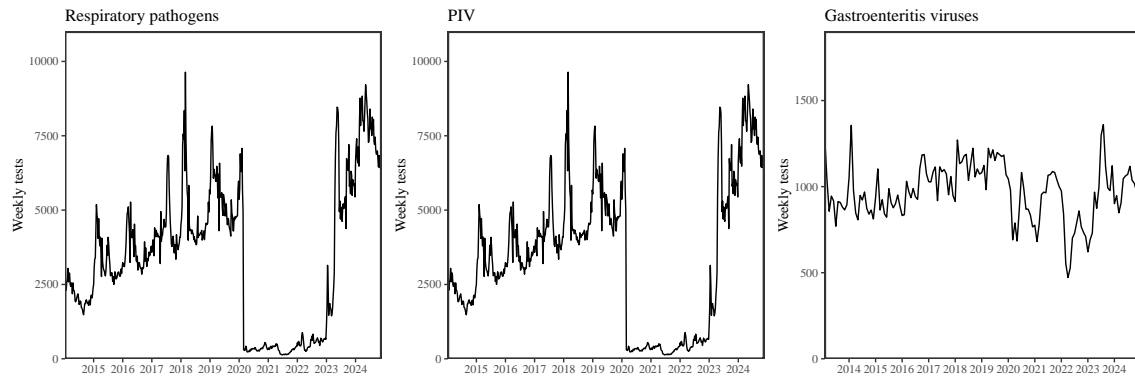


Figure S17: Testing patterns for respiratory pathogens, PIV, and gastroenteritis viruses in Hong Kong.

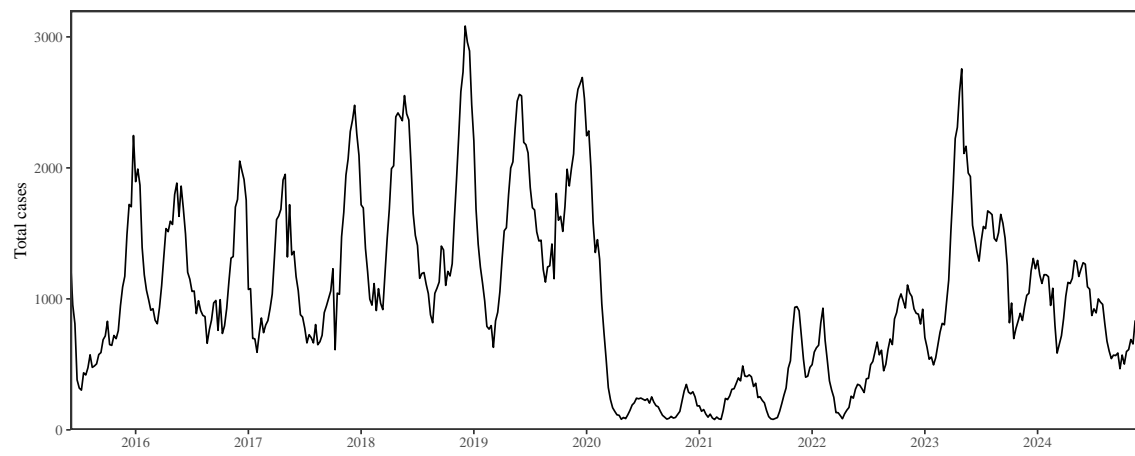


Figure S18: Total number of reported respiratory infection cases in Korea.

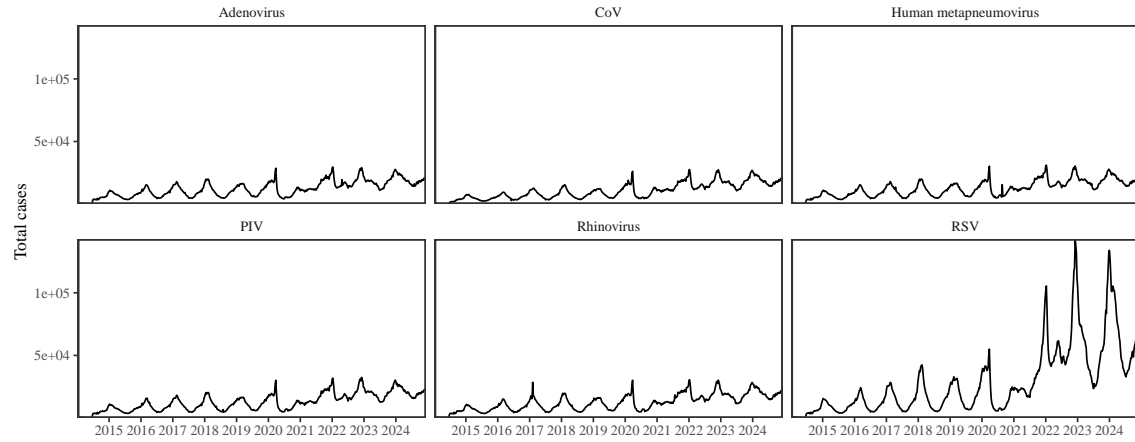


Figure S19: Testing patterns for respiratory pathogens in the US reported through the NREVSS.

739 References

- 740 [1] Rachel E Baker, Sang Woo Park, Wenchang Yang, Gabriel A Vecchi, C Jessica E
741 Metcalf, and Bryan T Grenfell. The impact of COVID-19 nonpharmaceutical
742 interventions on the future dynamics of endemic infections. *Proceedings of the*
743 *National Academy of Sciences*, 117(48):30547–30553, 2020.
- 744 [2] Gabriela B Gomez, Cedric Mahé, and Sandra S Chaves. Uncertain effects of the
745 pandemic on respiratory viruses. *Science*, 372(6546):1043–1044, 2021.
- 746 [3] Mihaly Koltai, Fabienne Krauer, David Hodgson, Edwin van Leeuwen, Marina
747 Treskova-Schwarzbach, Mark Jit, and Stefan Flasche. Determinants of RSV
748 epidemiology following suppression through pandemic contact restrictions. *Epi-*
749 *demics*, 40:100614, 2022.
- 750 [4] Sang Woo Park, Brooklyn Noble, Emily Howerton, Bjarke F Nielsen, Sarah
751 Lentz, Lilliam Ambroggio, Samuel Dominguez, Kevin Messacar, and Bryan T
752 Grenfell. Predicting the impact of non-pharmaceutical interventions against
753 COVID-19 on *Mycoplasma pneumoniae* in the United States. *Epidemics*,
754 49:100808, 2024.
- 755 [5] Amanda C Perofsky, Chelsea L Hansen, Roy Burstein, Shanda Boyle, Robin
756 Prentice, Cooper Marshall, David Reinhart, Ben Capodanno, Melissa Truong,
757 Kristen Schwabe-Fry, et al. Impacts of human mobility on the citywide trans-
758 mission dynamics of 18 respiratory viruses in pre-and post-COVID-19 pandemic
759 years. *Nature communications*, 15(1):4164, 2024.
- 760 [6] Eric J Chow, Timothy M Uyeki, and Helen Y Chu. The effects of the COVID-19
761 pandemic on community respiratory virus activity. *Nature Reviews Microbiol-*
762 *ogy*, 21(3):195–210, 2023.
- 763 [7] Stephen M Kissler, Christine Tedijanto, Edward Goldstein, Yonatan H Grad,
764 and Marc Lipsitch. Projecting the transmission dynamics of SARS-CoV-2
765 through the postpandemic period. *Science*, 368(6493):860–868, 2020.
- 766 [8] Rachel E Baker, Chadi M Saad-Roy, Sang Woo Park, Jeremy Farrar, C Jessica E
767 Metcalf, and Bryan T Grenfell. Long-term benefits of nonpharmaceutical inter-
768 ventions for endemic infections are shaped by respiratory pathogen dynamics.
769 *Proceedings of the National Academy of Sciences*, 119(49):e2208895119, 2022.
- 770 [9] Maaike C Swets, Clark D Russell, Ewen M Harrison, Annemarie B Docherty,
771 Nazir Lone, Michelle Girvan, Hayley E Hardwick, Leonardus G Visser, Pe-
772 ter JM Openshaw, Geert H Groeneveld, et al. SARS-CoV-2 co-infection with
773 influenza viruses, respiratory syncytial virus, or adenoviruses. *The Lancet*,
774 399(10334):1463–1464, 2022.

- 775 [10] Chun-Yang Lin, Joshua Wolf, David C Brice, Yilun Sun, Macauley Locke,
776 Sean Cherry, Ashley H Castellaw, Marie Wehenkel, Jeremy Chase Crawford,
777 Veronika I Zarnitsyna, et al. Pre-existing humoral immunity to human common
778 cold coronaviruses negatively impacts the protective SARS-CoV-2 antibody re-
779 sponse. *Cell host & microbe*, 30(1):83–96, 2022.
- 780 [11] Sam M Murray, Azim M Ansari, John Frater, Paul Klenerman, Susanna
781 Dunachie, Eleanor Barnes, and Ane Ogbe. The impact of pre-existing cross-
782 reactive immunity on SARS-CoV-2 infection and vaccine responses. *Nature*
783 *Reviews Immunology*, 23(5):304–316, 2023.
- 784 [12] John-Sebastian Eden, Chisha Sikazwe, Ruopeng Xie, Yi-Mo Deng, Sheena G
785 Sullivan, Alice Michie, Avram Levy, Elena Cutmore, Christopher C Blyth,
786 Philip N Britton, et al. Off-season RSV epidemics in Australia after easing
787 of COVID-19 restrictions. *Nature communications*, 13(1):2884, 2022.
- 788 [13] Stuart L Pimm. The structure of food webs. *Theoretical population biology*,
789 16(2):144–158, 1979.
- 790 [14] Michael G Neubert and Hal Caswell. Alternatives to resilience for measuring
791 the responses of ecological systems to perturbations. *Ecology*, 78(3):653–665,
792 1997.
- 793 [15] Lance H Gunderson. Ecological resilience—in theory and application. *Annual*
794 *review of ecology and systematics*, 31(1):425–439, 2000.
- 795 [16] Vasilis Dakos and Sonia Kéfi. Ecological resilience: what to measure and how.
796 *Environmental Research Letters*, 17(4):043003, 2022.
- 797 [17] Floris Takens. Detecting strange attractors in turbulence. In *Dynamical Sys-*
798 *tems and Turbulence, Warwick 1980: proceedings of a symposium held at the*
799 *University of Warwick 1979/80*, pages 366–381. Springer, 2006.
- 800 [18] Jonathan Dushoff, Joshua B Plotkin, Simon A Levin, and David JD Earn.
801 Dynamical resonance can account for seasonality of influenza epidemics. *Pro-*
802 , 101(48):16915–16916, 2004.
- 803 [19] Alan Hastings, Karen C Abbott, Kim Cuddington, Tessa Francis, Gabriel Gell-
804 ner, Ying-Cheng Lai, Andrew Morozov, Sergei Petrovskii, Katherine Scran-
805 ton, and Mary Lou Zeeman. Transient phenomena in ecology. *Science*,
806 361(6406):eaat6412, 2018.
- 807 [20] Matthew B Kennel, Reggie Brown, and Henry DI Abarbanel. Determining
808 embedding dimension for phase-space reconstruction using a geometrical con-
809 struction. *Physical review A*, 45(6):3403, 1992.

- 810 [21] Eugene Tan, Shannon Algar, Débora Corrêa, Michael Small, Thomas Stemler,
811 and David Walker. Selecting embedding delays: An overview of embedding
812 techniques and a new method using persistent homology. *Chaos: An Interdis-*
813 *ciplinary Journal of Nonlinear Science*, 33(3), 2023.
- 814 [22] Jennifer M Radin, Anthony W Hawksworth, Peter E Kammerer, Melinda Bal-
815 ansay, Rema Raman, Suzanne P Lindsay, and Gary T Brice. Epidemiology
816 of pathogen-specific respiratory infections among three US populations. *PLoS*
817 *One*, 9(12):e114871, 2014.
- 818 [23] Guojian Lv, Limei Shi, Yi Liu, Xuecheng Sun, and Kai Mu. Epidemiological
819 characteristics of common respiratory pathogens in children. *Scientific Reports*,
820 14(1):16299, 2024.
- 821 [24] Saverio Caini, Adam Meijer, Marta C Nunes, Laetitia Henaff, Malaika Zounon,
822 Bronke Boudewijns, Marco Del Riccio, and John Paget. Probable extinction of
823 influenza b/yamagata and its public health implications: a systematic literature
824 review and assessment of global surveillance databases. *The Lancet Microbe*,
825 2024.
- 826 [25] Zhiyuan Chen, Joseph L-H Tsui, Bernardo Gutierrez, Simon Busch Moreno,
827 Louis du Plessis, Xiaowei Deng, Jun Cai, Sumali Bajaj, Marc A Suchard,
828 Oliver G Pybus, et al. COVID-19 pandemic interventions reshaped the global
829 dispersal of seasonal influenza viruses. *Science*, 386(6722):eadq3003, 2024.
- 830 [26] Bryan T Grenfell, Ottar N Bjørnstad, and Bärbel F Finkenstädt. Dynamics of
831 measles epidemics: scaling noise, determinism, and predictability with the TSIR
832 model. *Ecological monographs*, 72(2):185–202, 2002.
- 833 [27] Samit Bhattacharyya, Per H Gesteland, Kent Korgenski, Ottar N Bjørnstad,
834 and Frederick R Adler. Cross-immunity between strains explains the dynamical
835 pattern of paramyxoviruses. *Proceedings of the National Academy of Sciences*,
836 112(43):13396–13400, 2015.
- 837 [28] Virginia E Pitzer, Cécile Viboud, Vladimir J Alonso, Tanya Wilcox, C Jessica
838 Metcalf, Claudia A Steiner, Amber K Haynes, and Bryan T Grenfell. Environ-
839 mental drivers of the spatiotemporal dynamics of respiratory syncytial virus in
840 the United States. *PLoS pathogens*, 11(1):e1004591, 2015.
- 841 [29] Katharine R Dean, Fabienne Krauer, Lars Walløe, Ole Christian Lingjærde, Bar-
842 bara Bramanti, Nils Chr Stenseth, and Boris V Schmid. Human ectoparasites
843 and the spread of plague in Europe during the Second Pandemic. *Proceedings*
844 *of the National Academy of Sciences*, 115(6):1304–1309, 2018.
- 845 [30] Margarita Pons-Salort and Nicholas C Grassly. Serotype-specific immunity
846 explains the incidence of diseases caused by human enteroviruses. *Science*,
847 361(6404):800–803, 2018.

- 848 [31] Sarah Cobey and Edward B Baskerville. Limits to causal inference with state-
849 space reconstruction for infectious disease. *PLoS one*, 11(12):e0169050, 2016.
- 850 [32] Public Health Agency of Canada. Respiratory virus detections in
851 Canada. 2024. <https://www.canada.ca/en/public-health/services/surveillance/respiratory-virus-detections-canada.html>. Accessed Sep
852 4, 2024.
- 854 [33] Centre for Health Protection. Detection of pathogens from respiratory spec-
855 imens. 2024. <https://www.chp.gov.hk/en/statistics/data/10/641/642/2274.html>. Accessed Nov 20, 2024.
- 857 [34] Centre for Health Protection. Detection of gastroenteritis viruses from faecal
858 specimens. 2024. <https://www.chp.gov.hk/en/statistics/data/10/641/717/3957.html>. Accessed Nov 20, 2024.
- 860 [35] Korea Disease Control and Prevention Agency. Acute respiratory infection,
861 Sentinel surveillance infectious diseases. 2024. <https://dportal.kdca.go.kr/pot/is/st/ari.do>. Accessed Nov 20, 2024.
- 863 [36] Edward Goldstein, Sarah Cobey, Saki Takahashi, Joel C Miller, and Marc Lipsitch.
864 Predicting the epidemic sizes of influenza A/H1N1, A/H3N2, and B: a
865 statistical method. *PLoS medicine*, 8(7):e1001051, 2011.
- 866 [37] Bob Carpenter, Andrew Gelman, Matthew D Hoffman, Daniel Lee, Ben
867 Goodrich, Michael Betancourt, Marcus A Brubaker, Jiqiang Guo, Peter Li,
868 and Allen Riddell. Stan: A probabilistic programming language. *Journal of
869 statistical software*, 76, 2017.
- 870 [38] Stan Development Team. RStan: the R interface to Stan, 2024. R package
871 version 2.32.6.